Engineering Structures 292 (2023) 116534

Contents lists available at ScienceDirect

Engineering Structures

journal homepage: www.elsevier.com/locate/engstruct

Structural design and engineering of Striatus, an unreinforced 3D-concrete-printed masonry arch bridge

A. Dell'Endice *, S. Bouten, T. Van Mele, P. Block

ETH Zurich, Institute of Technology in Architecture, Zurich, Switzerland

ARTICLE INFO

Keywords:
Unreinforced masonry
Discrete element modelling
3D printing
Funicular form finding
Digital fabrication

ABSTRACT

This paper describes the structural design and engineering of "*Striatus*", a 3D-concrete-printed unreinforced masonry pedestrian bridge built in Venice in 2021 as part of the Time Space Existence exhibition organised by the European Cultural Centre. The project combines the latest developments in 3D concrete printing with the structural principles of historic unreinforced masonry. Typically, the structural applications of 3D concrete printing are limited to elements such as columns and walls loaded vertically, perpendicularly to the horizontal printing layers, to formwork elements or secondary structural elements. Indeed, fabrication constraints, delamination issues and the low tensile strength of the concrete have been seen as limiting factors to 3D concrete printing for structural applications demanding resistance to bending or predominant loading directions not perpendicular to the printing layers. By using unreinforced-masonry structural principles, this paper shows that structural elements spanning space horizontally, such as a pedestrian bridge, can be built by using the 3D concrete printing components as the main structure, working only in compression, loaded perpendicularly to the printed layers. Furthermore, as a compression-only structure following masonry principles, Striatus enabled the use of unreinforced concrete without any mechanical or chemical connections between the elements and the separation of concrete and steel, only used for the supports and to equilibrate the horizontal thrust of the arch effect through the tension ties. This work shows how the application of unreinforced masonry principles to 3D concrete printing offers new opportunities in terms of structural design and represents a strategy to increase sustainability by reducing material consumption and allowing reusability and recyclability of the structure. Finally, this paper discusses the critical aspects related to the design of Striatus from an engineering and construction point of view.

1. Introduction

The growth of large-scale 3D concrete printing (3DCP) in the Architectural, Engineering and Construction (AEC) industry raises questions about the structural applications achievable with additive manufacturing. Despite the advantages in terms of geometry and fabrication, the mechanical properties of the raw material are not entirely preserved in the printing process. The layer-by-layer fabrication makes the mechanical behaviour orthotropic, with higher strength in the direction perpendicular to the printed layers than the direction parallel to the printing plane. Indeed, the bonding between the layers constitutes a weak point, causing delamination, and depends on several parameters such as printing speed, material fluidity and composition [1–9].

For all these reasons, the 3D concrete printing of structural applications has been limited to vertical columns or walls [10,11], with the addition of reinforcement steel elements [12], or as lost formwork (outer shell) for concrete casting [13]. In other cases, 3D-concrete-printed components have been used as secondary structural elements of pedestrian bridges, whose main structure is made of steel components, or post-tensioned with printed layers not orthogonal to the flow of forces [14,15]. Recently, researchers in 3DCP have been investigating and proposing several strategies for the production of 3DCP elements spanning space horizontally: Nubian or other forms of vaulting [16–18], with the integration of reinforcements during printing to achieve some bending capacity for short spans [19,20], printing perpendicular to stress lines [21,22] or using lost formwork in different materials [23].

However, the limited development of structural applications for 3D-concrete-printed components should also be associated with using structural design principles developed for materials such as reinforced

* Corresponding author.
E-mail address: dellendice@arch.ethz.ch (A. Dell'Endice).

https://doi.org/10.1016/j.engstruct.2023.116534

Fig. 1. The Striatus bridge, Giardini della Marinaressa, Venice 2021. Photo credits: (c)naaro.

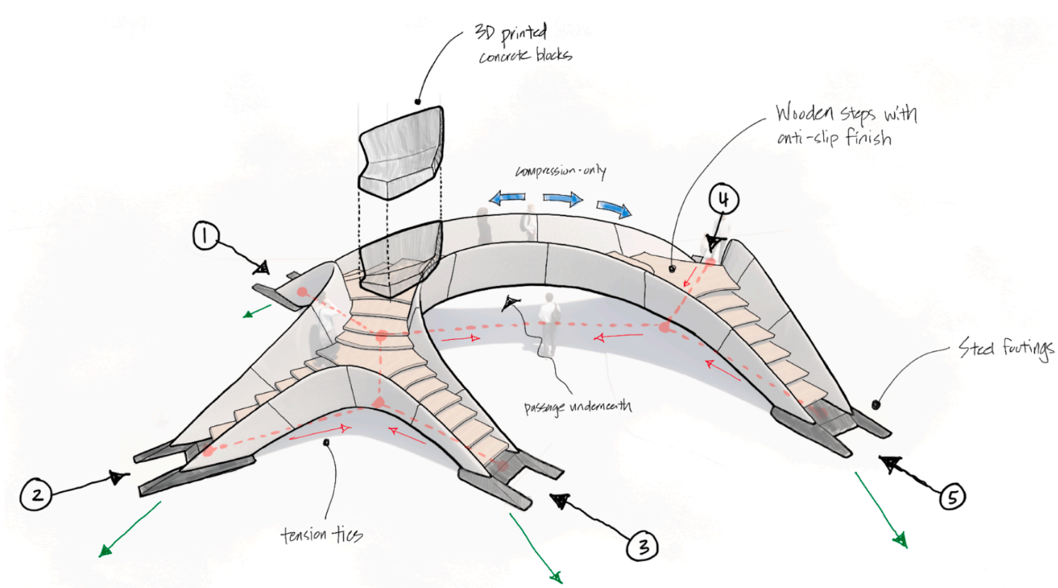

Fig. 2. Sketch describing the design principles of Striatus. Image credits: Juney Lee.

concrete, steel or wood [24]. Nevertheless, due to the similar behaviour of 3DCP components with materials only resistant to compression, traditional structural principles of historic unreinforced masonry (URM) structures can be applied [25,26].

1.1. Striatus

Striatus is a 3D concrete printed unreinforced masonry pedestrian bridge built in the Giardini della Marinaressa in Venice, during the Venice Architecture Biennale 2021, hosted by the European Cultural Centre, Fig. 1, [27].

Striatus uses a discrete stereotomic structural system inspired by traditional unreinforced masonry structures to overcome the limitations of 3DCP and produce a 16 m-span pedestrian arch bridge built entirely out of unreinforced 3D-printed concrete components, assembled without steel reinforcements or mechanical connections between the blocks. This project aims to demonstrate that fabrication-informed structural design allows realising strength through structural geometry, in which, combined with common-sense construction logic, materials are used in a way that they want to be used. This opens up the design space of environmentally responsible solutions to several possibilities in creating and exploring efficient and expressive shapes.

Striatus has been developed by the Block Research Group (BRG) at ETH Zurich and Zaha Hadid Architects Computation and Design Research Group (ZHCODE) in collaboration with Incremental3D and Holcim.

The sketch in Fig. 2 shows the design logic of Striatus: multiple arches in compression assembled from 3D-printed concrete voussoirs supported by steel footings on concrete pads connected by steel tension ties to resolve the horizontal thrust of the funicular form.

1.2. URM principles and 3D concrete printing

Several reasons make URM structural principles suitable for 3D concrete printing components. URM structures are composed of discretised elements kept together in equilibrium mainly because of their spatial geometrical arrangement and stereotomy. The materials of the elements composing URM structures are usually unilateral (only resistant in compression), such as stones or bricks (e.g., fired clay, ceramics), while their shapes (stereotomy) follow precise geometrical rules, which foster a compression-only flow of forces within the structure. As a result, most of these structures experience low stress and do not require any reinforcement. The design of URM structures has been developed throughout the centuries considering all these aspects. Traditional structural typologies have evolved, and countless URM buildings still stand and constitute most of the residential and monumental buildings worldwide.

In 3D concrete printing, the material is also unilateral. As well known, concrete has excellent resistance to compression but a limited tensile capacity. Depending on the printing setup employed or the geometric complexity of the component to be printed, the additive manufacturing process brings advantages in terms of shapes, since no formworks or moulds are needed. In the case of 3D concrete printing with nozzles mounted on huge gantries, the dimensions of the 3D printed components can be large, but the three-dimensional design freedom is usually limited. This technology is usually used to construct walls or columns with parallel horizontal layers. Instead, with robotic 3D concrete printing using two-component (2 K) mix setups, more freedom is provided by the multiple movement axes of robotic arms [28]. In this last case, the design freedom is a trade-off between the possibilities offered by the robotic arm, the properties of the "ink" used for the printing in terms of workability, bonding between layers, curing time, and the computational geometry generation pipeline. By adding material only where it is needed for structural or functional requirements, it is possible to reduce material consumption. In Striatus, up to 50% of the cross-section of each component is hollow. Applying URM principles to 3D concrete printing, discretised compression-only structures can be realised with significant design freedom, saving material and offering improved sustainability since no high compressive strengths are required. Furthermore, the Striatus project shows how four R's of circularity can be applied to concrete [27]:

1. Repair: longevity is achieved by exploiting the "natural" geometry required by the material mechanical properties, avoiding the damages inducted by the corrosion of embedded reinforcement bars.
2. Reduce: with additive manufacturing and structurally informed geometry, the material is placed only where needed, using less material and eliminating single-use materials for the fabrication.
3. Reuse: dry assembled structures can be easily dismantled, and this has an important outlook for concrete prefabricated components, which can be then re-employed in other structures.
4. Recycle: since the concrete is unreinforced, so without embedded rebar or fibres, each component can be recycled with minimal energy cost.

1.3. Computational structural tools

The structural design of URM structures requires specific tools to evaluate the relevant aspects contributing to the equilibrium of such a structural typology. Currently, in structural engineering, most of the methods employed for designing new structures are based on the strength of the material, which is not the main concern for URM structures [29]. Only a few are suitable for the design of URM structures and capable of dealing with complex three-dimensional geometries. In the design of URM structures, geometry represents the main contributing factor to the structure's equilibrium at both global and local levels. The global geometry should provide natural paths for the funicular flow of forces, while the elements' discretisation, namely their stereotomy, should ensure the minimisation of the shear components of the contact forces at the interfaces. Historically, the massive thickness of URM structures, together with their geometry, ensured that the stress level was one or more orders of magnitude lower than the strength of the material, rarely representing a concern [29]. However, in the current structural design context, the requirements for sustainability lead toward a reduction of material consumption and optimised cross-sections, which are facilitated by additive manufacturing fabrication methods. Thus, local structural checks on the material working stress rate could be required in this case.

The design of new URM structures is very limited in the AEC industry. Most structural methods dealing with URM are for the stability assessment of existing historical buildings, but their use for complex three-dimensional geometries is a challenge for both assessment and design. For the structural design and engineering of Striatus, an ad-hoc computational pipeline was developed with COMPAS [30], combining several packages and enabling a smooth workflow throughout the entire process, from the design and form finding to the engineering and the fabrication and construction. In particular, the URM structural logic has been designed and analysed using *compas_3dec* [31], a package for the structural assessment and design of complex three-dimensional URM structures based on the Discrete Element Modelling (DEM) method, using the commercial DEM software 3DEC by Itasca as a backend solver [[32–34]. *compas_3dec* is part of COMPAS Masonry [35], an open-source, Python-based computational framework for the practical assessment of URM structures. It bundles different solvers using a common data management system, *compas_assembly*. *compas_assembly* provides a fast, direct and robust way to handle complex assemblies of discrete parts and manage their interfaces and interactions. *compas_3dec* provides functions to quickly input discrete geometries in 3DEC, with the possibility of dealing with concave blocks and propagating specific distributions of geometrical and mechanical imperfections through the digital model. Furthermore, *compas_3dec* allows the post-processing of 3DEC results, visualising changes in the flow of forces within the structure due to variations of the boundary conditions and other features relevant for the assessment and design of URM structures.

1.4. Discrete Element Modelling

For a few decades, the DEM method has been used for the structural analysis of engineering problems dealing with discrete bodies (soil mechanics, particles, masonry, etc.) with several applications in masonry structures [36–39]. The motion of the blocks is described by Newton's second law and solved numerically by the central difference method with respect to a scalar parameter (e.g., time). The position of the blocks during the calculation is updated step by step. Two different kinds of analyses are possible, static and dynamic, and both are solved with explicit numerical algorithms. Static analyses are performed introducing damping in the equation of motion. The three main peculiarities of this method are that i) the discretised elements can move and deform independently; ii) large displacements are possible; and, iii) the blocks can detach from each other or form new contacts. These features make it suitable for the structural assessment and design of unreinforced masonry structures [[40,41]. Indeed, in DEM, Heyman's fundamental assumptions on the material masonry [29] can be approximated, namely: unlimited compressive strength, no tensile strength, and no sliding [37,42,43]. However, DEM is not bound to limitations coming from the no-sliding assumption and a finite value of the interface friction angle has to be defined to run the analysis. The next chapter describes the form finding and the global equilibrium calculation of Striatus.

2. Form finding and equilibrium analysis

This chapter describes the form finding and the equilibrium analysis of Striatus. The entire process has been done iteratively, starting by

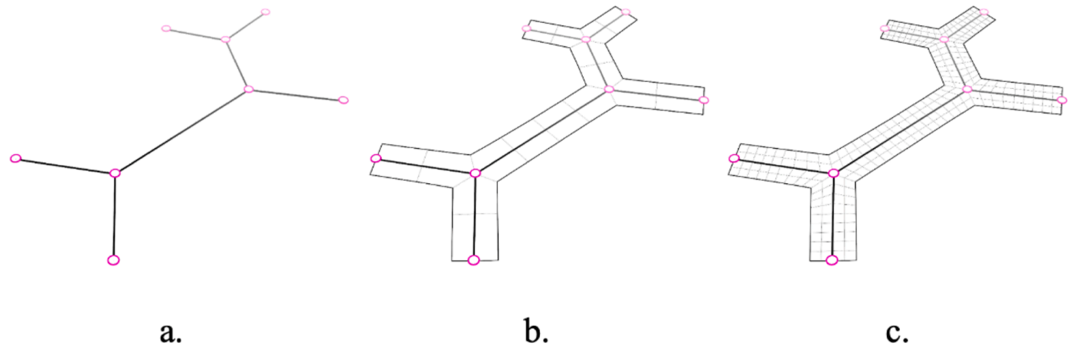

Fig. 3. Parametric geometry generation: a) skeletal graph; b) coarse starting mesh; c) subdivided mesh.

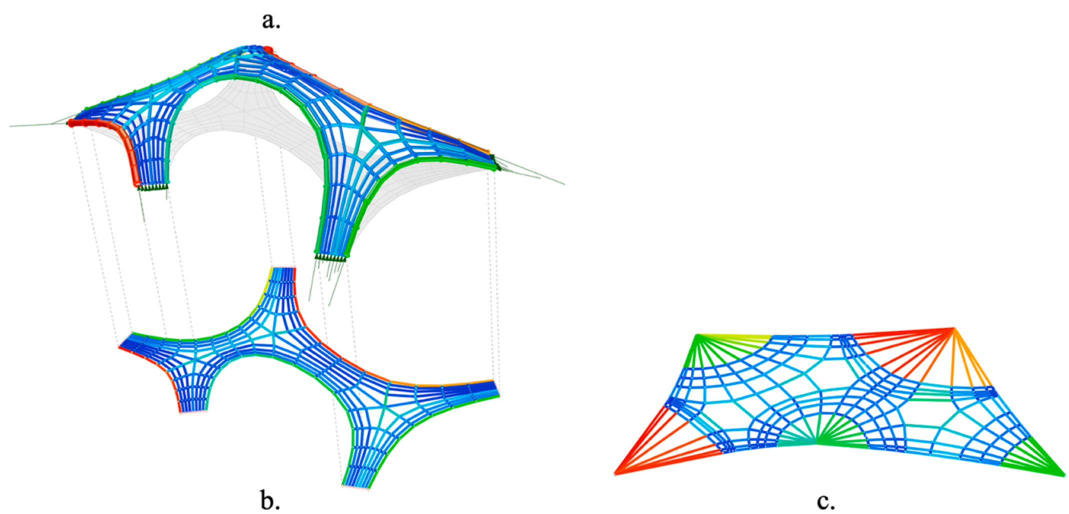

Fig. 4. TNA form finding of the deck's mesh: **a)** thrust network; **b)** form diagram; and **c)** force diagram.

building a parametric data structure of the geometry. Later, the same geometric data were smoothly exchanged among the tools used for the design, form finding and equilibrium analysis, allowing the evaluation of several design alternatives.

The initial sketch of Striatus was realised considering constraints related to i) the 3D-printing fabrication process, ii) the structural principles of funicular URM structures, and iii) the site conditions of the Giardini della Marinaressa in Venice. COMPAS mesh and network data structures were used to describe the geometry. During the structural design phase, these data structures have been enriched with mechanical data and used by different software without compatibility issues. The form finding and equilibrium analysis of Striatus is the result of combining three main tools: *compas_tna,* which implements the Thrust Network Analysis (TNA) method [44,45], *compas_3dec*, and the commercial FEA software *Sofistik*.

2.1. Input geometry

The input geometry of the bridge was designed starting with a skeletal graph that connects the five supports and corresponds to the centreline of the deck. Then, a 2D mesh was generated from this centreline graph and further subdivided, forming the initial form diagram for the TNA form finding described in the next section, Fig. 3. This initial mesh generation only involved the deck's geometry; the balustrade meshes were developed in a successive phase. This interactive geometry generation pipeline, from a skeletal graph to a hi-res mesh, was used to iteratively refine the starting mesh to accommodate the design constraints (dimensions, supports' locations, site).

2.2. Thrust network analysis

The 2D mesh designed in the previous step has been used as a form diagram for the structural form finding based on the TNA method, which generates a 3D thrust network of compressive forces in equilibrium with a predefined set of loads (Fig. 4). Once the arched shape of the deck was form-found, it was modified considering specific architectural constraints and requirements, such as the slope of the ramps. The geometrically modified 3D mesh of the deck was then structurally re-evaluated to restore the compression-only thrust network using a best-fit algorithm [46], which uses the modified mesh as the target shape and tries to find a compression-only thrust network as close as possible to the target. Due to the complexity of the bifurcating deck's geometry, with five supports and four spans of irregular shape between them, the best-fit procedure was iteratively applied to define a smooth distribution of the forces, which has a direct effect on the slope of the surface towards the supports.

As expected, the evaluation of the TNA results of the deck's structure shows a 3D shell behaviour with arch action in both directions, predominantly from support to support, but secondary in the short dimensions of the deck, in between the open edges. However, this theoretical compression-only shell behaviour is only possible if the discretisation of the materialised structure allows the same force distribution. The form-found mesh was then materialised, i.e., given thickness and a discretisation/stereotomy, and analysed using the DEM method, as described in the next section.

2.3. Materialisation: Thickness and discretisation

The form-found mesh was used as the middle surface of the deck,

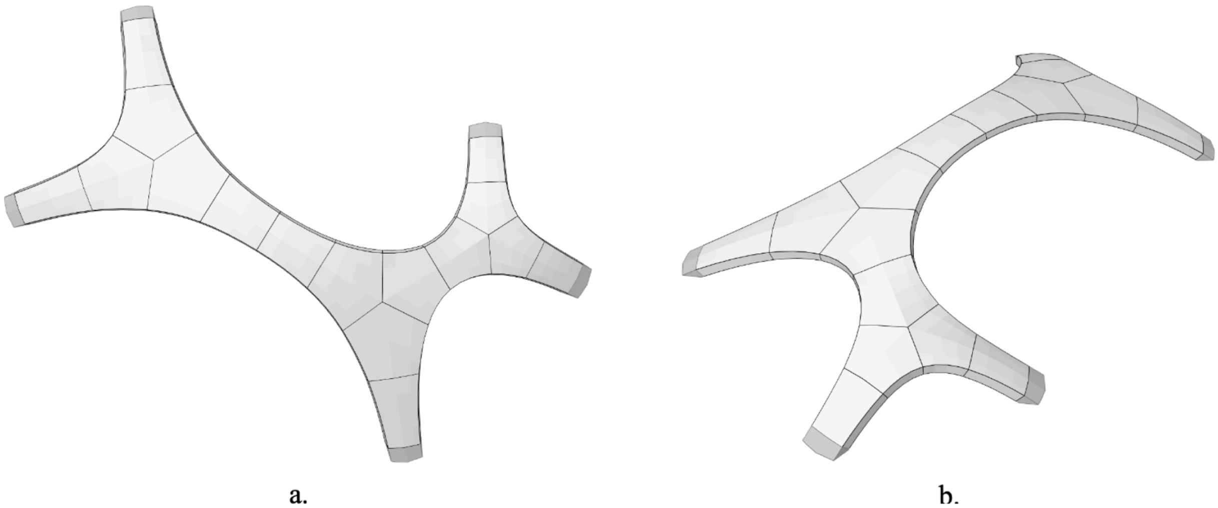

Fig. 5. The deck's geometry after materialisation and discretisation, **a)** top view; **b)** perspective view.

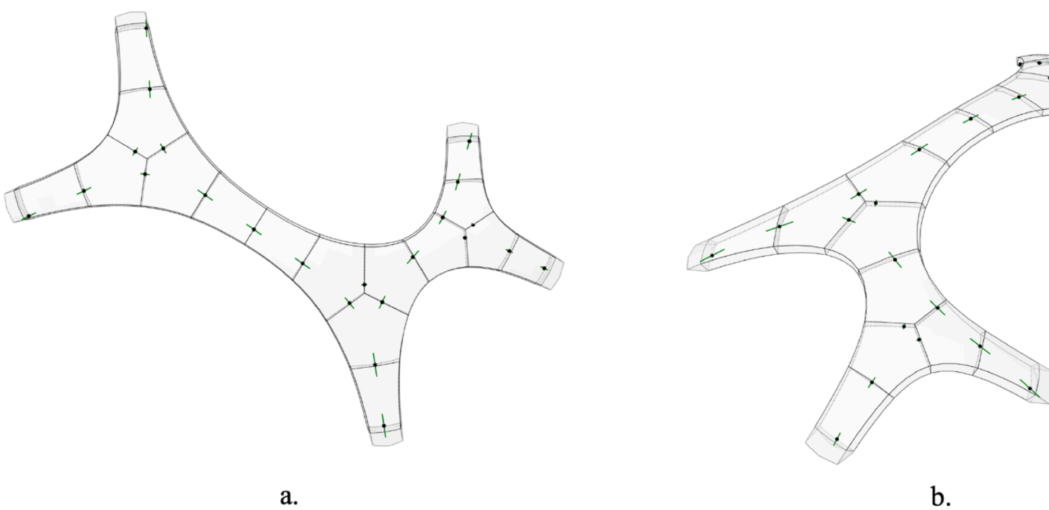

Fig. 6. Global equilibrium of the deck: visualisation of the resultant interface forces through *compas_3dec,* **a)** top view; **b)** perspective view.

from which the intrados and extrados were defined using a variable offset. An initial thickness considered the minimum thickness achievable by the 3D printing process. This minimum thickness was assigned to the elements in the centre of the main span and increased toward the supports. Later, the second part of the materialisation process involved the discretisation of the deck geometry, which together with the thickness of the elements constitute essential parameters for the stability of masonry structures. Indeed, stereotomy plays a fundamental role in the structural behaviour, in particular in the distribution of the flow of forces within them, and it must result in joints as perpendicular as possible to the main compression forces (Fig. 5).

To achieve this, the joints between the deck blocks were first defined perpendicular to the intrados surface of the structure. Then, the discretisation and its spacing were defined considering constraints related to the 3D-printing process (mainly the maximum angle achievable between the starting and ending printing planes, as explained in Section 2.4.3), and the manoeuvrability of the printed components during transportation and assembly (weight and dimensions). For each discretisation, the flow of forces was computed and visualised using *compas_3dec*. The position of the resultant contact forces with respect to the thickness of the interfaces and the magnitude of their shear components were evaluated. At the locations where the shear components of the contact forces reached values close to the maximum shear force allowed by the friction angle, the stereotomy was improved by modifying the inclination of the interfaces resulting in a reduction of the shear components. No mechanical (pins or clamps) or chemical (glue or mortar) connections were used at the interfaces between the elements in order to keep the characteristic behaviour of URM structures, resulting in dry joints. Neoprene pads were added between the 3D-printed components in order to improve the force distribution over the interfaces, reducing the chance for stress concentration due to possible fabrication imperfections, interface roughness or misalignments due to assembly imprecisions. The following paragraph describes the DEM analysis conducted using *compas_3dec*.

2.4. *Discrete Element Modelling*

The Discrete Element Modelling (DEM) analysis has been conducted approximating Heyman's assumptions about the mechanical behaviour of unreinforced masonry structures [29]. Rigid blocks have been used, which implies unlimited compressive strength, and the Mohr-Coulomb failure criterion has been adopted to describe the joints' behaviour, where tensile strength, cohesion and dilatancy angle have been set to zero to replicate the dry joints with no tensile capacity. The no-sliding theoretical condition applied to URM structures mainly derives from an attentive design of the 3D stereotomy, which makes the normal

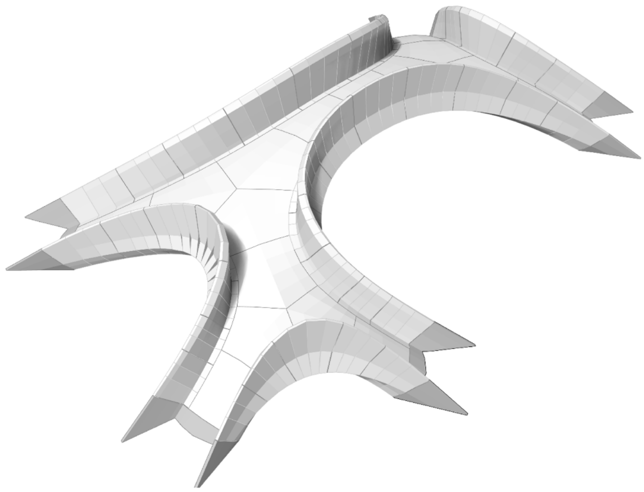

Fig. 7. Perspective view of the entire bridge geometry.

components of the interface contact forces predominant compared to the tangential ones. In the DEM software 3DEC, by modelling the geometry three-dimensionally, the effect of the stereotomy is taken into account, and the interface friction angle value can be defined based on the material properties of the joints. In the case of Striatus, the joints' behaviour considers the mechanical properties of the thin neoprene pads inserted between the 3D-printed components, which have been taken into account in the calculation of the joint stiffness values, normal and shear, calculated as described by [38].

2.4.1. DEM mechanical parameters

This section describes the mechanical parameters adopted in the DEM analysis. The density of the 3D-printed concrete material was taken as 2400 kg/m^3, but since the blocks are hollow, with a solid-to-empty ratio of about 60% of the total volume, the density is reduced to 60% of the initial value, so 1500 kg/m^3. The Young's Modulus of the 3D-printed material was determined from four-point bending tests, resulting in 42 GPa, while the interface friction angle value used was 25° (derived from the static friction coefficient neoprene-concrete measured in [47]). For almost all the joints, the neoprene pads used are 6 mm thick, except for those between the steel supports and the first 3D-printed components, and those at the singularities (pentagonal blocks), which have a thickness of 8 mm. The thicker pads have been used at the supports since the compressive forces reach their maxima at those locations. At the singularities, instead, due to the geometric complexity of the pentagonal blocks, the thicker pads help to provide full contact at the interfaces and buffer potential geometric deviations. The calculated Young's Modulus of the neoprene pads, which has been used for the calculation of the joint stiffness values, is 0.003 GPa, while the Shear Modulus is 0.001 GPa. For the steel of the supports, a density of 7850 kg/m^3 was used.

2.4.2. Deck's design

As expected, the global equilibrium of the materialised deck shows that the adopted stereotomy does not allow the same force distribution shown by TNA (Fig. 6**)**. Indeed, by only cutting the deck in the direction perpendicular to the boundary arches, the forces mainly flow normally to the joints, and there is no significant arch effect in the deck's short dimension, which is minimal and only visible through a finite element analysis of the printed components. The DEM analysis shows that the deck is a stable structure by itself, i.e., without the balustrade elements. Through *compas_3dec,* the positions of the resultant contact forces with respect to the thickness of the deck's components were checked, and the geometry (curvature, thickness and discretisation) was adjusted to have the forces flow as close as possible to the middle surface of the deck.

2.4.3. Balustrade's design

Once the deck's geometry was defined, the balustrade arches were designed, considering several aspects, Fig. 7:

1. unreinforced masonry principles for the block's stereotomy;
2. staggered pattern with respect to the deck blocks;
3. 3D-printing process constraints;
4. architectural requirements for minimum height and shape of the handrail;
5. interface orientation between balustrade and deck components.

Regarding point 1), the balustrades were treated as arches, which according to URM principles, need to be formed as wedged-shaped blocks to maximise the normal components of the contact forces. In the case of Striatus, due to the overall inclination of the balustrades, the 3D-printed components are wedged-shaped both in plan as in section, as shown in Fig. 8.

Points 2) and 3), instead, helped define the dimensions and geometry of the balustrade blocks. Indeed, the block's length is related to the discretisation of the deck, forming a staggered pattern, which allows the components to engage their neighbours three-dimensionally, like in traditional URM, and avoids the formation of continuous hinging lines within the structure. The defined blocks' dimensions and discretisation were double-checked with the constraints coming from the 3D-printing production process. Indeed, the wedged-shaped blocks have a non-parallel ending printing plane with respect to the horizontal starting printing plane. The 3D-printing process, with inclined layers of variable thickness, posed constraints on the maximum angle between these two

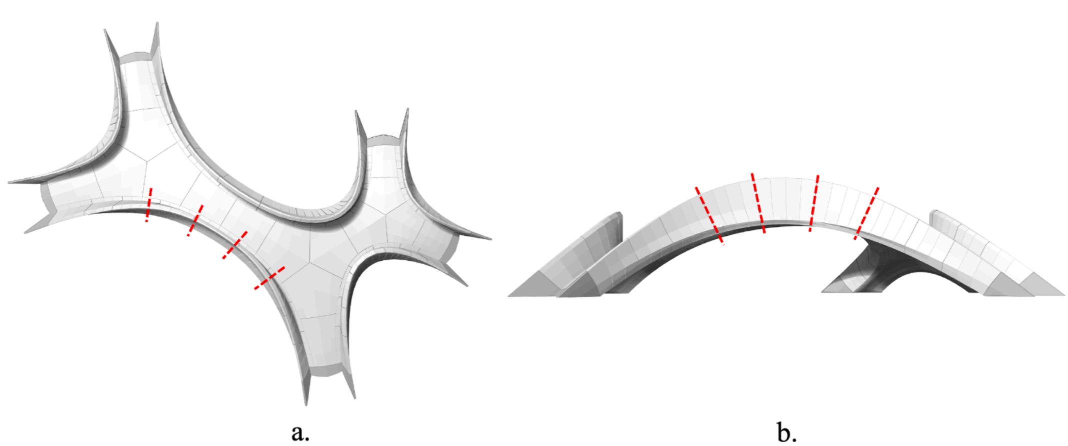

Fig. 8. Alignment of wedged-shaped balustrade voussoirs in **a)** top view, and **b)** side view.

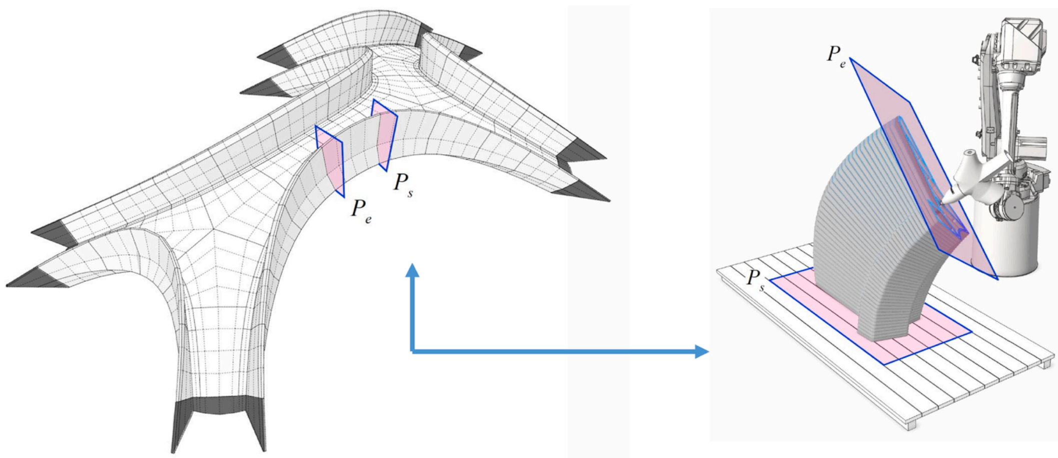

Fig. 9. Start and end planes of a wedge-shaped balustrade component.

Fig. 10. Balustrade cross section: wider at the bottom to increase the "structural depth" for the in-plane components of the thrust, thinner at the top for the handrail function.

planes (Fig. 9**)**.

For point 4), since the 3D-printed components of the balustrade arches serve as a handrail, architectural requirements about their height and width were considered. At the middle point of the bridge's main span, the handrail has a height of 1.05 m, which was gradually reduced towards the supports. The cross sections of the balustrade components have been designed thinner at the top, where they function as handrails (0.05 m) than at the bottom, where structural depth is needed to catch the in-plane components of the thrust lines flowing within the arch (0.5–0.6 m), Fig. 10. Indeed, the arch's geometry of the balustrades can take in-plane loads, but they require lateral stability from the deck to be fully in equilibrium, as described next in Point 5.

The last aspect of the balustrade design (point 5) involved the analysis of the interaction between the deck structure and the balustrade arches. In a first design attempt, considering the cross-section of the bridge at the middle span (Fig. 11), the interfaces between deck and balustrade components were first intuitively designed to follow the typical stereotomy of a vault arching in two directions. Fig. 11**a**. This decision was driven by the initial intent to design a 3D vault, which was form found using TNA, with forces flowing in both principal directions along the main arches and in the short dimension of the deck, as previously shown in Fig. 4.

However, as previously shown in Fig. 6, the deck is a stable structure by itself, and the contact forces predominantly flow in the main arching direction, perpendicular to the joints. So, the deck structure does not rely on the support of the balustrade arches to be stable. The deck exerts no thrust on the balustrade arches. In fact, it is the balustrade arches that need to be stabilised laterally by leaning and pushing against the central deck, balanced by the opposite action of the leaning balustrade arch on the other side. Indeed, the DEM analysis of the structure using the initial interface angle (Fig. 11**a)** showed that for such a discretisation the lateral stability of the balustrade arches heavily relies on the friction capacity of the interfaces. In many locations, the shear components of the resultant contact forces were close to or reached the limit allowed by the theoretical friction capacity. Moreover, it was clear that perfect contact conditions between the deck and the balustrade components could not be guaranteed due to imprecisions in the printing and assembly processes. Those would reduce the effective contact surfaces, causing precarious contact conditions or increasing stress concentrations. As a natural, albeit surprising, conclusion, the inclination of the interfaces between the deck and balustrades were reversed (Fig. 11**b)**, decreasing the shear components of the contact forces at the interface between the deck and balustrade blocks. *compas_3dec* allowed us to identify this issue because of the clear visualisation of the shear components of the contact forces.

2.4.4. Final geometry and structural working principles

After defining the deck and balustrade geometries, the entire structure has been analysed in *compas_3dec*, checking the contact forces, their positions and characteristics. The final design of Striatus is composed of two main systems, the bifurcating deck, which is stable by itself and the balustrade arches, which need the deck for their lateral stability. The presence of inclined arches pushing laterally against the deck also increases the deck's stability against horizontal loads. The specific three-dimensional shape and stereotomy of Striatus, with five supports and multiple staggered structural elements interacting with each other, add redundancy to the structure, allowing the three-dimensional redistribution of the load paths in multiple directions. The 3D force distribution is also facilitated by the pentagonal blocks designed at the deck's singularities (where the deck's skeleton changes its direction), which redirects the flow of forces towards the supports. Computed using *compas_3dec*, Fig. 12 shows the contact forces within the geometry of Striatus due to self-weight, illustrating the actions of the bifurcating deck arch, the balustrade arches and the interaction between them. The lengths of the green lines in Fig. 12 are proportional to the forces' magnitude. At the supports, the resultant thrusts are represented with arrows. The position of the resultants, calculated by the DEM analysis, is

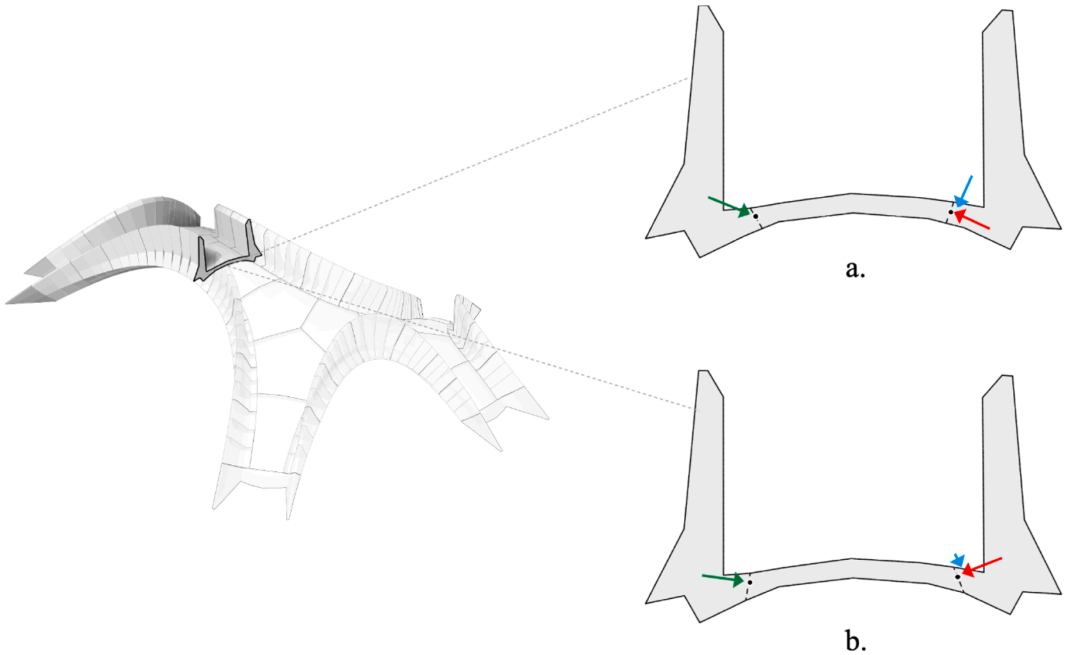

Fig. 11. Deck/balustrade interface design. In green, red and light cyan respectively the force exerted by the balustrade on the deck, its normal and shear components: **a)** initial deck/balustrade interface angle; **b.** interface angle used for Striatus. (For interpretation of the references to colour in this figure legend, the reader is referred to the web version of this article.)

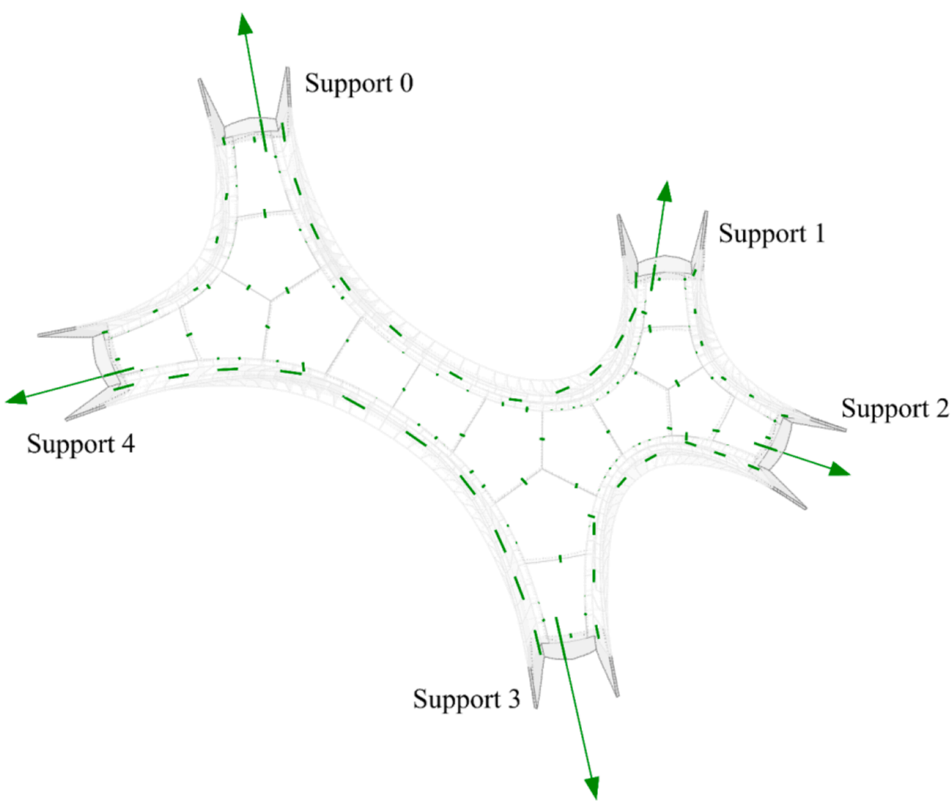

Fig. 12. Flow of forces due to self-weight within Striatus computed by *compas_3dec*.

not perfectly aligned with the tension ties, which run at the ground level following the skeleton of the geometry, as described in Chapter 4 about the foundation system. However, the solution found by 3DEC, due to the indeterminacy of the structural system, is only one of the infinite solutions compatible with the boundary conditions. For this reason, ground screws have been installed at the base of the supports to take any remaining force components, which could cause rotation, Fig. 27.

3. Settlements and load cases

After the geometry was defined and the global equilibrium of Striatus under its self-weight verified, the structural design continued using

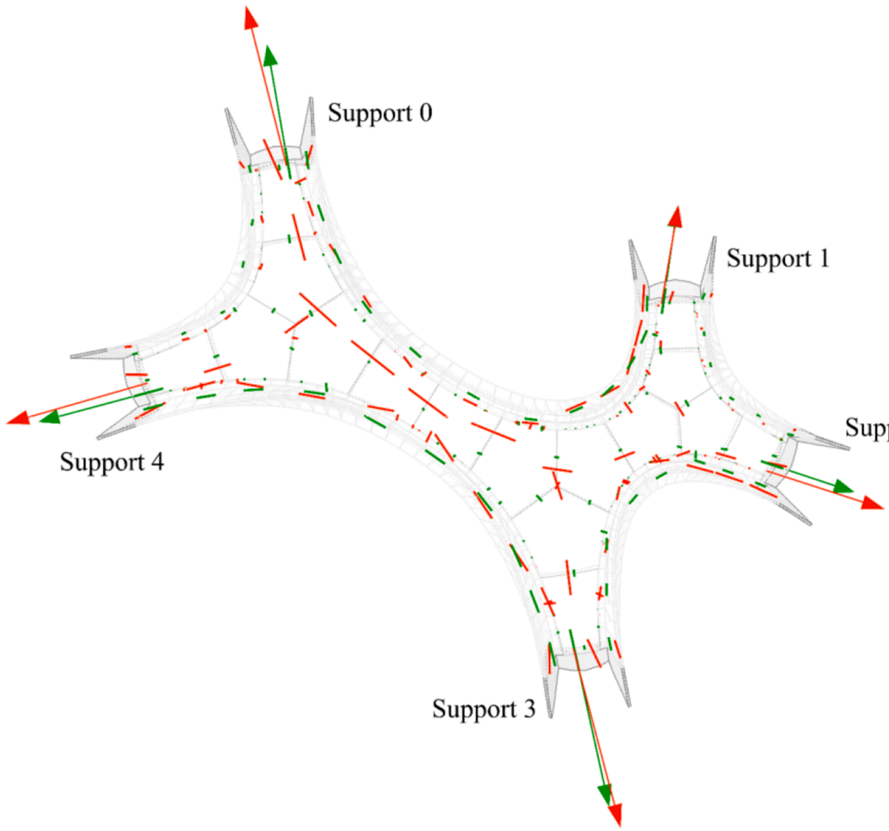

Fig. 13. Comparison of the force flow due to self-weight (in green) and after applying an outward displacement to the supports (in red). (For interpretation of the references to colour in this figure legend, the reader is referred to the web version of this article.)

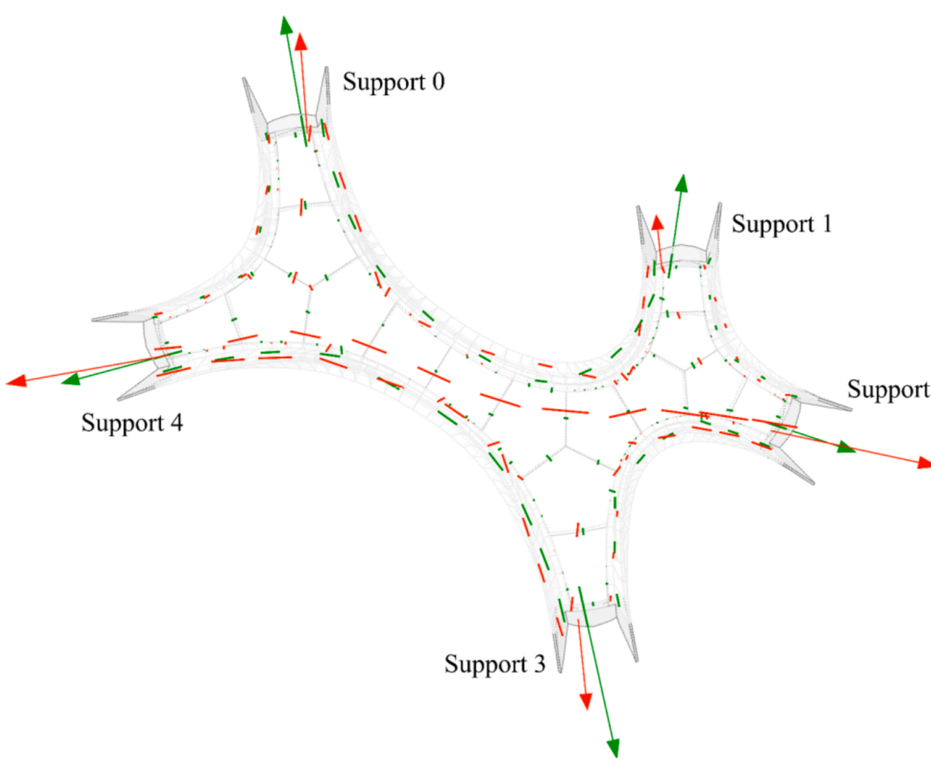

Fig. 14. Comparison of the force distribution before (in green) and after vertical displacement of Support 3 (in red). (For interpretation of the references to colour in this figure legend, the reader is referred to the web version of this article.)

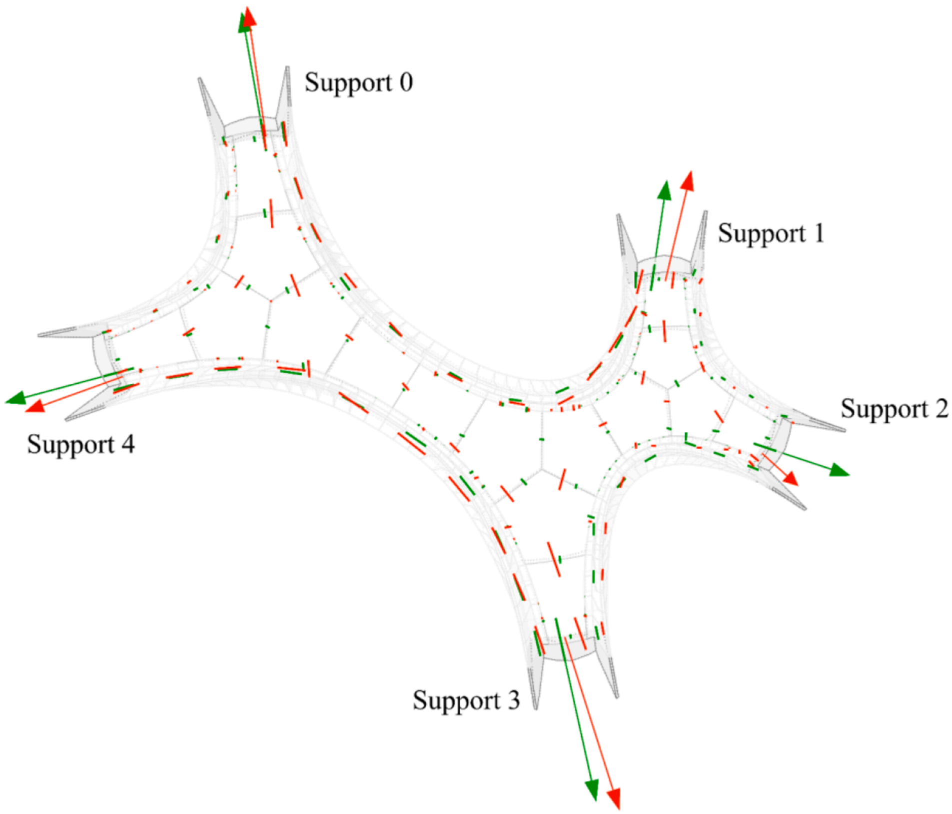

Fig. 15. Comparison of the force distribution before (in green) and after vertical displacement of Support 2 (in red). (For interpretation of the references to colour in this figure legend, the reader is referred to the web version of this article.)

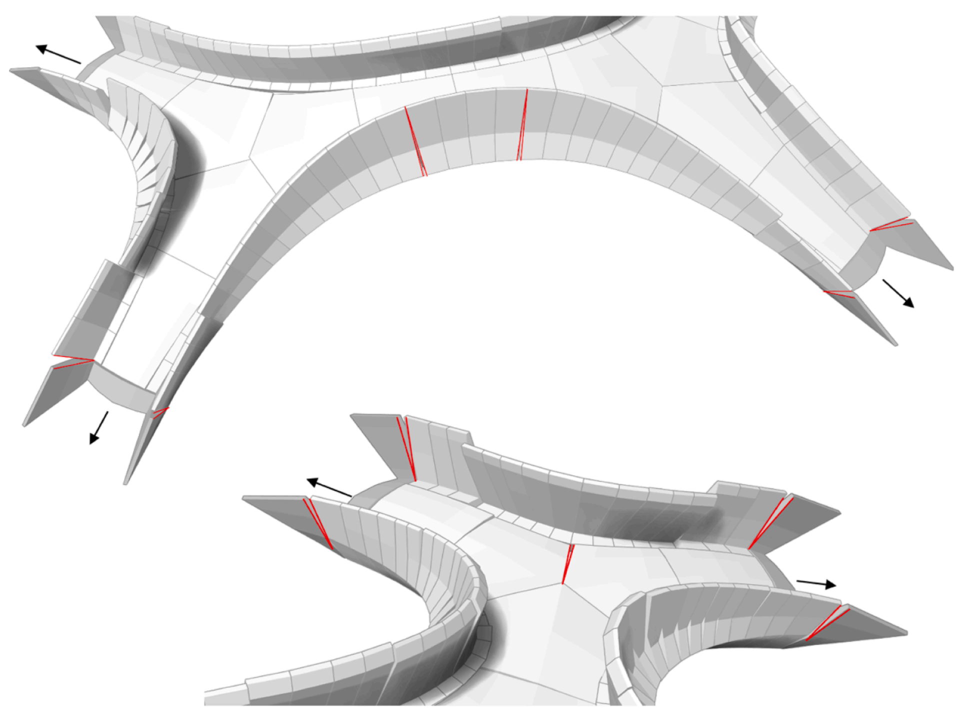

Fig. 16. Deformed configuration before collapse due to an outward displacement of 0.166 m of each support.

compas_3dec, evaluating the effects on the structure of differential settlements of the supports and of several load cases.

3.1. Settlements

In historic URM structures, settlements, and, more generally, displacements are the most frequent cause of damage, which could lead to

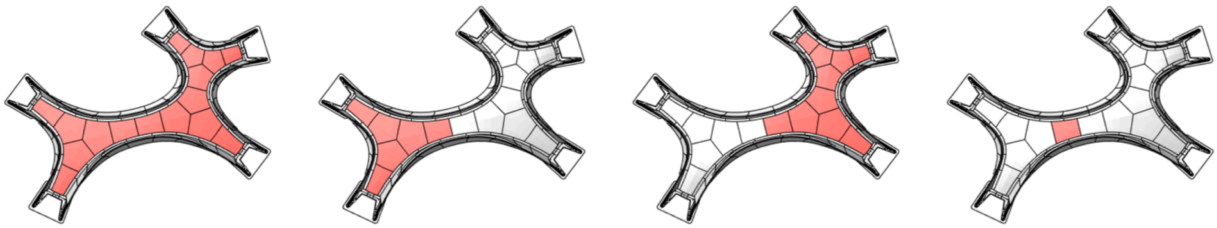

Fig. 17. Red areas representing the distributed load cases analysed: **a)** full deck; **b)** left half; **c)** right half; **d)** single block. (For interpretation of the references to colour in this figure legend, the reader is referred to the web version of this article.)

collapse [Heyman 1966]. However, due to their discrete nature, URM structures can accommodate relatively large displacements through the opening and closing of hinges in between blocks. As a result, the displacement capacity can reach significant values before the hinges form a collapse mechanism [39,48,49]. In the case of Striatus, the steel tension ties connecting the five supports and the ground screws below each foundation pad discourage any horizontal displacement of the supports. However, due to the poor mechanical properties of the soil in the Giardini della Marinaressa gardens in Venice, where the bridge was located, vertical and outwards settlements of the supports have been simulated to understand: i) the level of safety of the structure, ii) the kinematics of an eventual failure mechanism due to settlements, iii) and the capacity of the structure to redistribute the loads in case of differential settlements.

The DEM method is suitable for this type of analysis, and thanks to *compas_3dec,* the behaviour of the entire structure can be carefully observed and evaluated. Therefore, three different support displacements have been analysed, neglecting the presence of the tension ties and ground screws and considering plausible scenarios compatible with the limited bearing capacity of the soil. The cases analysed are i) the spreading of all the supports in the directions of the bridge's resultant forces due to self-weight (Fig. 13); ii) vertical settlement of the support receiving the highest resultant force (Support 3) (Fig. 14); and, iii) a vertical settlement of the support at the end of the main span (Support 2 in Fig. 15). The expected maximum vertical settlement per support, calculated considering the loads, the properties of the foundation without considering the bearing capacity of the ground screws installed underneath the reinforced concrete foundation pads (Fig. 27**)** and the mechanical properties of the soil, was approximately 0.015 m. The much larger displacement capacity of the structure obtained from the DEM simulation of the vertical settlements, as shown in sections 3.1.2 and 3.1.3 resulted in a safety factor equal to 17.

3.1.1. Outward displacement of all supports:

Each of the five supports was moved outwards in steps of 0.001 m, along the direction of the resultant force due to the structure's self-weight at that support. This was considered the most probable direction of an outward displacement in case, e.g., the tension ties were to be damaged. The maximum outward displacement capacity obtained was 0.166 m per support. In Fig. 13, the flow of forces without support displacements (in green) is compared to the one resulting from the outward displacement of the supports (in red), where on average, the magnitude of the contact forces is bigger. Indeed, after decreasing to minimal thrust, further outward displacements cause an increase of the horizontal forces due to the reduction of the rise of the main arch and in turn of the effective vertical lever arm.

As a consequence of the moved foundations, hinges form within the structure (Fig. 16), and the flow of forces must pass through them.

The two close-ups in Fig. 16 show the hinging locations marked with red lines and the deformed shape of the balustrade arches. In the initial configuration, the inclined balustrade arches are stable in their plane but require lateral stability from the deck structure. In the deformed configuration, after the outward displacement of the supports, hinges form, causing the rotation of the most inclined balustrade components around the hinges, namely the blocks in the middle. However, also in this case, the deck presence limits the rotations, keeping the arch stable and contributing to the large displacement capacity reached by the bridge. Fig. 16 shows that an eventual global failure of the structure due to settlements is always preceded by a gradual opening of cracks at the interfaces, which could be visually monitored.

3.1.2. Vertical settlement of support 3:

The vertical displacement of Support 3 was applied in increments of 0.001 m, and the value reached before collapse was 0.254 m. The visualisation of the contact forces highlights how the flow of forces changes within the structure due to the settlement, compared to the self-weight case (Fig. 14**)**. The stereotomy and discretisation allow the three-dimensional redistribution of the forces along a different path between Supports 2 and 4, avoiding Support 3, which is the one being lowered in the analysis, and for symmetry reasons also circumventing Support 1. Moreover, the redistribution increases the magnitude of the forces travelling in the deck, which is proportional to the length of the lines in Fig. 14.

3.1.3. Vertical settlement of support 2:

In this case, a simulation similar to ii) was done by vertically moving down Support 2 using the same increment per step (0.001 m). The maximum displacement reached before collapse is 0.252 m. Also, in this case, the contact forces are redirected towards the adjacent supports (1 and 4), but the flow of forces is not significantly affected since in the case without support displacements only a small proportion of the forces, compared to the other supports, travel towards Support 2. Indeed, the two flows illustrated in Fig. 15 are quite similar, except locally in the right part of the structure, where a slight redistribution is visible.

In conclusion, the analysis of the outward displacements and differential settlements has shown a large displacement capacity, which is above any expected or possible displacement of the supports or extension of the tension ties. On the other hand, the capacity to accommodate large deformations shows that an eventual failure of the structure does not result in a sudden collapse, but is always preceded by a gradual opening of hinges, which can be visually monitored (Fig. 16). These observed deformations could then be checked against the DEM simulations to estimate the most likely cause for them.

The analysis of the modified force flow due to the differential boundary displacements has highlighted the structure's capacity to three-dimensionally redistribute the contact forces, forming alternative paths still only working in compression. In the following section, the bridge's behaviour under several load cases is discussed.

3.2. Load cases

Multiple load conditions have been considered to address the Serviceability Limit State (SLS) and Ultimate Limit State (ULS). Starting from the analysis under self-weight (DL), several live load (LL), and

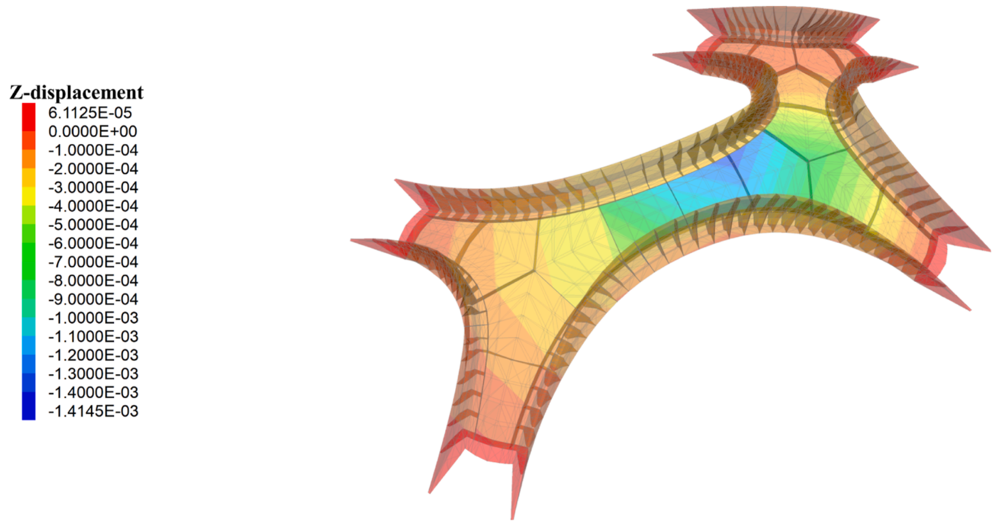

Fig. 18. Z-displacement values in m calculated by 3DEC after the application of a distributed load of 5 kN/m^2 on the entire deck surface.

Fig. 19. Loading test of Striatus: sandbags placed on the deck (left), and measurement of the deflections using LVDTs (right).

point load (PL) cases have been tested. For URM arch-shaped structures, the worst loading condition consists of loads applied asymmetrically with respect to the middle of the span. Asymmetric loads more easily cause the thrust line to exceed the structure's thickness and, consequently, the forming of hinges that could lead to collapse. The magnitude of the loads tested considered the Italian standards for public pedestrian bridges, as described below. The load cases have been subdivided into two categories: i) distributed loads and ii) point loads. Fig. 17 summarises the distributed load cases evaluated.

The required distributed load by the Italian standards for pedestrian bridges (NTC 2018 [50]) is 5 kN/m^2, but the simulation was carried up to higher values to investigate when the structure would become unstable and hinges would form a collapse mechanism. However, since DEM simulations with rigid blocks can only evaluate the global equilibrium of the structure, an FEM analysis using the commercial software *Sofistik* has been carried out to check the stress values and deformations of the material by considering the maximum values of the contact forces in between the 3D-printed components calculated by 3DEC. The contact forces have been translated to stress distributions and applied to the blocks in *Sofistik*, considering the locations of the resultant contact forces with respect to the interfaces and the material properties. The FEM analysis has been conducted on the digital model of the hollow geometry of the blocks, hence considering the actual thickness of the thin elements composing the 3DCP blocks. Fig. 18 describes the vertical displacement values in m calculated by 3DEC for load case a) of Fig. 17, where 5 kN/m^2 have been applied on the full area of the deck.

Similar values of z-displacements have been measured during the load test executed after the assembly of Striatus. The structure was loaded with sandbags and the deflections measured using Linear Variable Differential Transformers (LVDTs) placed against the intrados (the

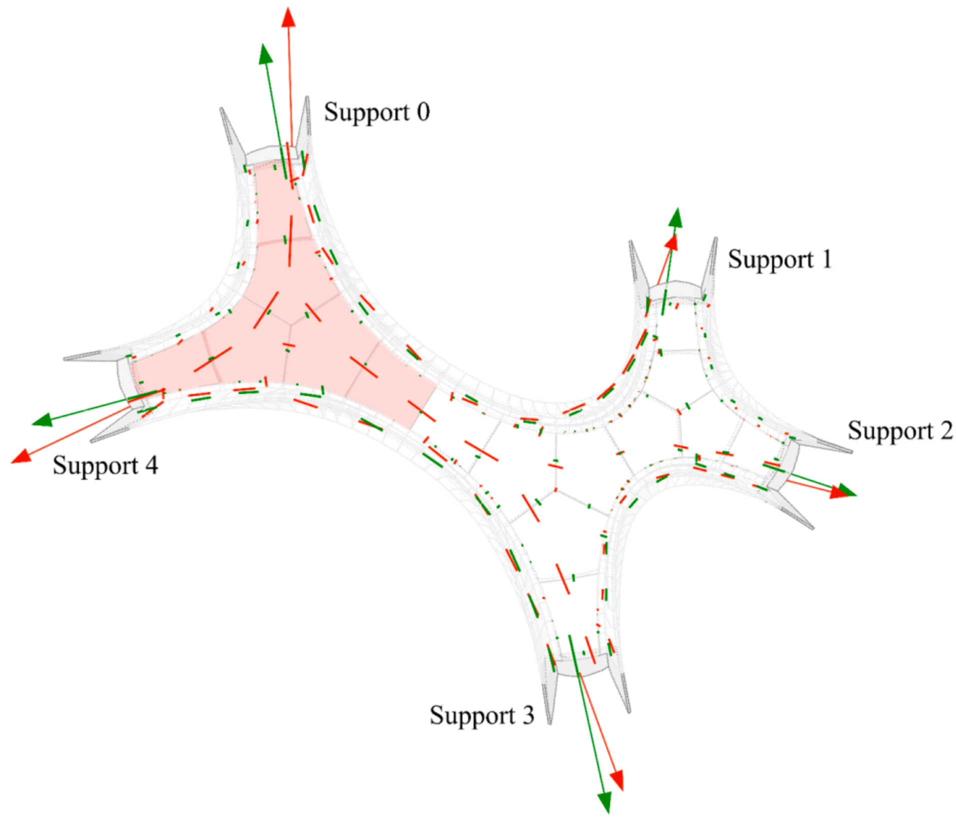

Fig. 20. Flow of forces visualised with *compas_3dec*: due to self-weight (in green); and, due to self weight + 5 kN/m^2, applied on the light red area on the deck's left half (in red). (For interpretation of the references to colour in this figure legend, the reader is referred to the web version of this article.)

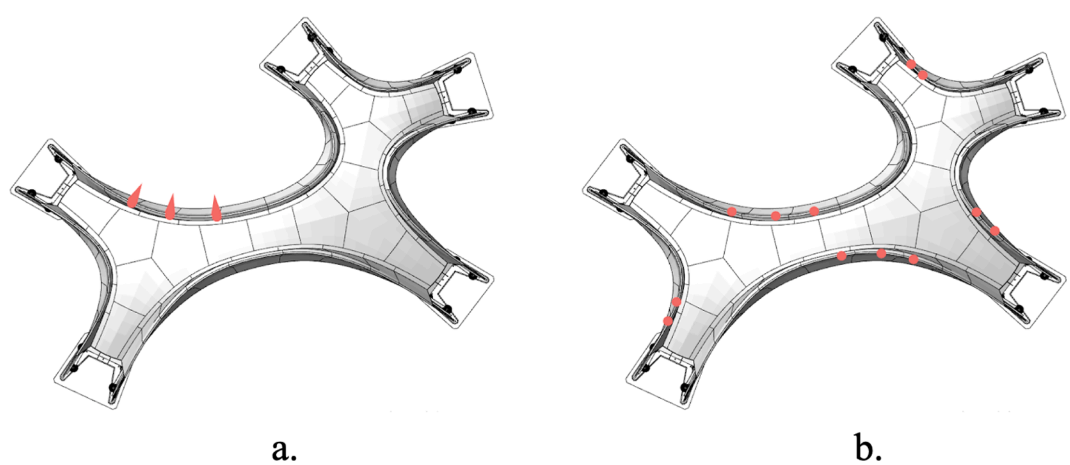

Fig. 21. Point loads applied to the balustrades: **a)** horizontal loads; and, **b)** vertical loads.

bottom surface) of the main span (Fig. 19). The comparison highlighted the reliability of the DEM analysis in describing the global structural behaviour of Striatus, in terms of displacements, due to the combination of the 3D-concrete-printed blocks and neoprene pads at the interfaces. The elastic behaviour of the neoprene, modelled in DEM by considering its Young's modulus in the calculation of the joint stiffness values, resulted in a slightly elastic behaviour of the bridge. Indeed, the bridge deflected during the loading procedure with sandbags, but it recovered almost entirely to its initial configuration as soon as it was unloaded. The joint stiffness values, normal and shear, which considered the deformability of both concrete and neoprene, have been calculated according to the equations specified by [38] for the calculation of the joint stiffness values in the case of mortared joints between stone blocks. In particular, the normal joint stiffness has been defined as:

$$J_{kn} = \left(d_b/E_{block} + t_n/E_{neoprene}\right)^{-1} \quad (1)$$

where d_b is the distance between two consecutive joints, E_{block} is the Young's modulus of the concrete, t_n is the thickness of the neoprene pad and $E_{neoprene}$ is the Young's modulus of the neoprene. While, the shear joint stiffness is defined by replacing the Young's modulus of the materials with their shear moduli G:

$$J_{ks} = \left(d_b/G_{block} + t_n/G_{neoprene}\right)^{-1} \quad (2)$$

All the mechanical properties of the materials are specified at the end of this paper in the **Appendix**.

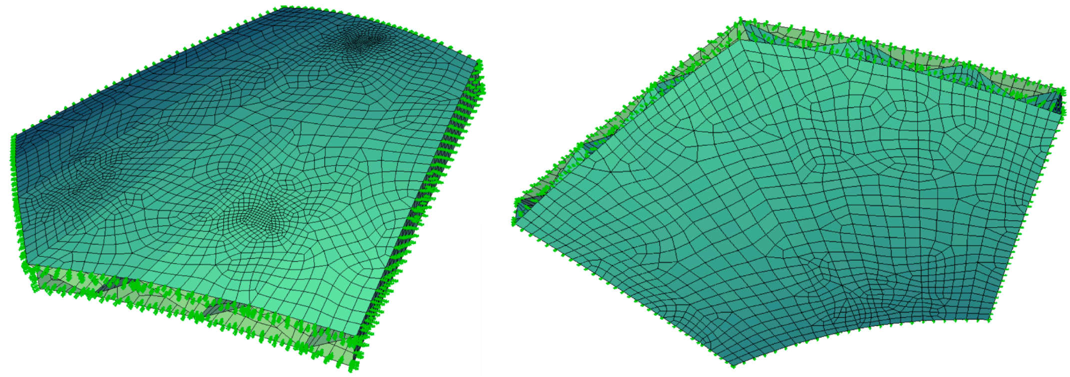

Fig. 22. Finite Element models in SOFiSTiK, mesh as 4-point surface elements.Densification of mesh at local load introduction, and support springs at interface nodes.

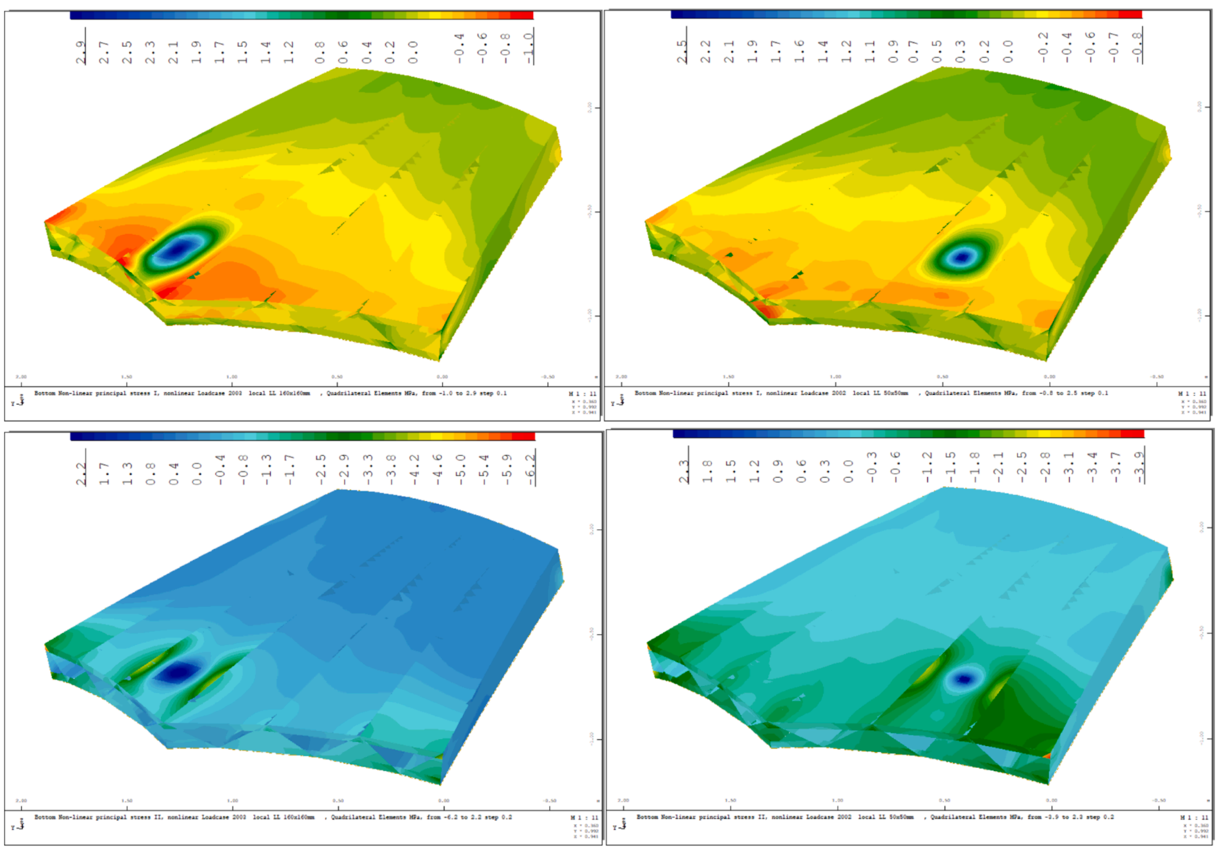

Fig. 23. Stress analysis in SOFiSTiK, showing principal stresses at the lower faces of the quad elements;

In the DEM simulations, none of the distributed load cases applied caused global instability, showing good capacity for redistributing loads three-dimensionally. Fig. 20 compares the flow of forces due to self-weight (in green) and after load applied to the left half of the deck, i. e., case b in Fig. 17 (in red).

The comparison clarifies how the discretisation enables the three-dimensional redistribution of asymmetric loads. Contact forces change their magnitude and position at the interfaces between the elements, and the resultant forces at the supports change their magnitude and lines of action, resulting in larger reactions at Supports 0 and 4, as can be expected because those provide the most direct load path for the surcharge to travel to the supports.

The structural analysis of Striatus also considered the application of point loads at the balustrade, as illustrated in Fig. 21. In the analyses, several point loads (2 kN each) were applied on the top of the balustrade's components in two directions, vertically downwards and horizontally perpendicular to the balustrade direction. The point loads applied to Striatus, calculated by 3DEC, did not show significant deflections. Indeed, due to the inclined shape of the balustrade arches, their structural depth and the compression forces travelling within them, both directions of point loads did not cause any issue to the stability of the structure, and all the thrust lines were fully contained in the thickness of the balustrade arches.

At this point, the global equilibrium of the materialised geometry under self-weight, spreading supports, differential settlements and distributed and concentrated load cases have been verified. In the next phase of the structural design, described in the following section, local checks on the stress levels have been conducted using FEM analysis, starting from the contact forces calculated by the DEM analysis.

Fig. 24. The cross-section shows the thicknesses of the printed layers and the triangulation.

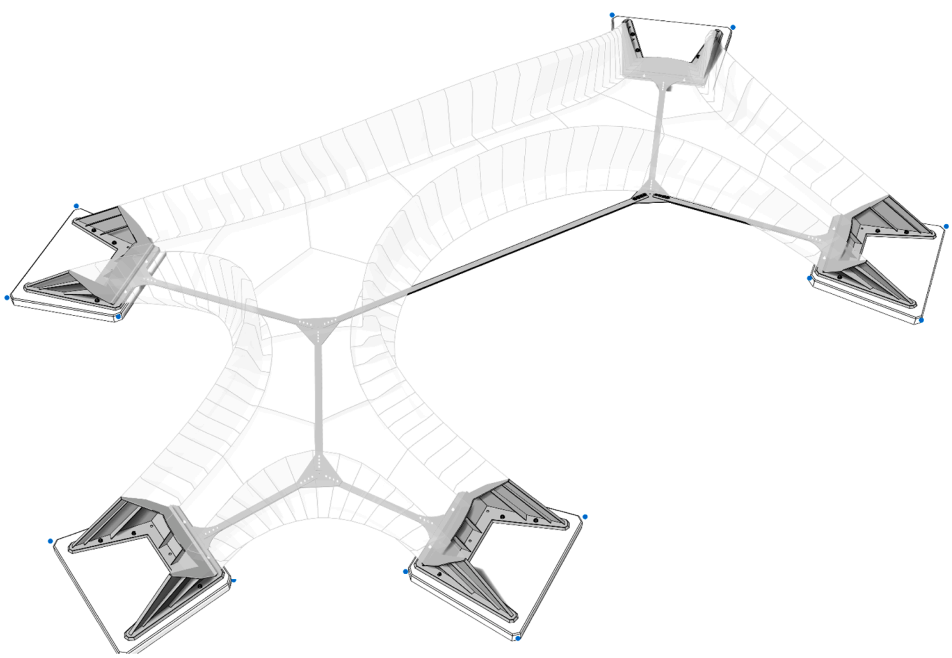

Fig. 25. Foundation system. Steel supports attached to the concrete pads and connected through tension ties.

3.3. FEM analysis

To complement the DEM analysis that verified the global equilibrium of simplified solid elements, detailed Finite Element (*FE*) models, which considered the hollow geometry of the blocks, were built to verify local stresses. Throughout the structural design process, these local verifications contributed to decisions about the triangulation scheme of the stiffeners inside the hollow elements and the required thickness of the 3D-printed layers, particularly the top surface of the bridge's deck blocks.

The FE models of single voussoirs were built in the SOFiSTiK analysis software [51], and implemented from 4-noded surface elements (*quads*). Local densifications of the finite element mesh were included at load introduction locations to ensure an adequate stress representation (Fig. 22).

The boundary conditions of the single voussoir models were represented by compression-only spring elements at the nodes that would lie on contact faces with other blocks. These spring elements were given a lateral Coulomb friction coefficient of 0.466, corresponding to a friction angle of 25°. Material properties for the mix were applied as given in the **Appendix**. It was decided to discard orthotropic stiffness properties in the model - a simplification that is justified by considering that the modelled higher bending stiffness across the printing layers attracts higher stresses along this critical direction. As the 3D-Printed concrete mix has a high compression strength capacity, the local design of the blocks is governed fully by tensile stresses. These can arise from bending and shear action due to punching loads, and as transverse tensile stresses due to material compatibility (Poisson ratio 0.21) under concentrated interface loads. Hence, it was verified that tensile stresses remained under their design resistance values (see **Appendix**) under the following

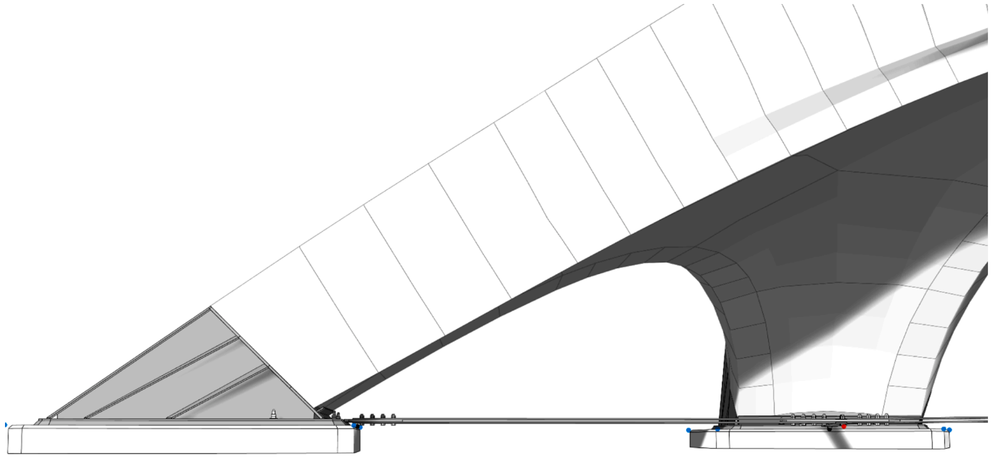

Fig. 26. Side view of the interface between the steel support and the last 3DCP block.

Fig. 27. Installation of the formwork for the concrete pads. This image shows the heads of the ground screws connected to the steel reinforcements cage before the concrete casting.

Fig. 28. The activated tension ties after removing the falsework/scaffolding system.

Fig. 29. Scaffolding system made of DOKA towers braced diagonally.

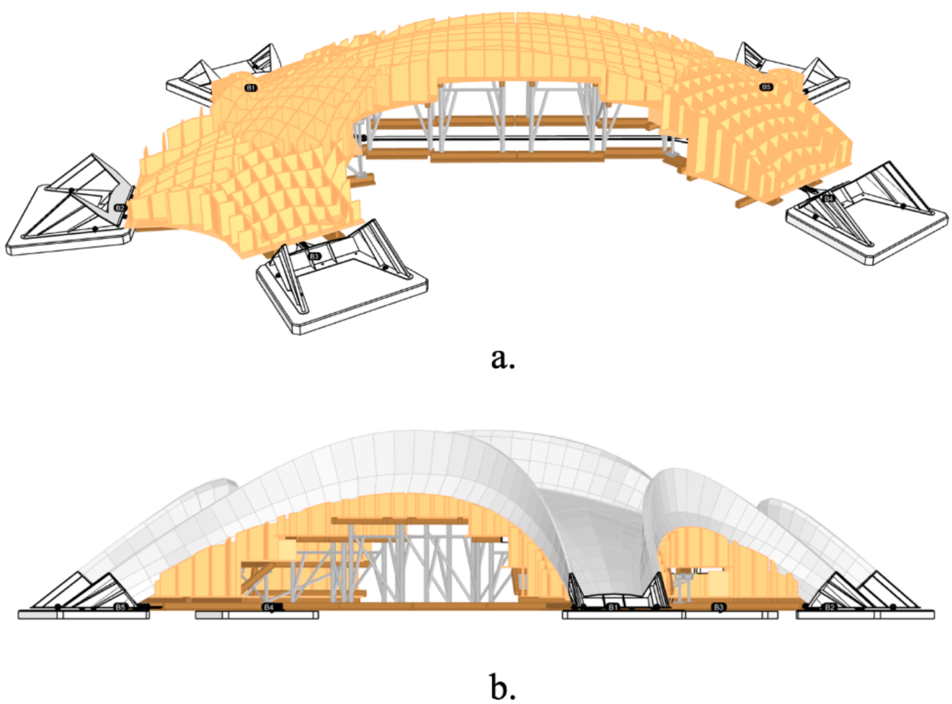

Fig. 30. Digital model of the wooden waffle system: **a)** waffle components on the top of the DOKA elements; **b)** 3D printed blocks placed on the waffle.

critical load cases (Fig. 23):

1. A concentrated live load of 4.0 kN (design value 6.0 kN), applied to a surface of 0.15 m × 0.15 m.This was applied only at the top of the deck blocks.
2. An accidental load of 2.0 kN (design value 3.0 kN), applied to a surface of 0.05 m × 0.05 m.This was applied at all locations, including bottom of deck blocks and balustrade blocks.
3. Concentrated interface loads applied along single edges, representing a hinged state.The load magnitudes were taken as the maximum interface forces from the DEM model.
4. Uniformly distributed live load on deck blocks of 5.0 kPa (design value 7.5 kPa).It was found that uniformly distributed loads were not governing for the local design.

due to concentrated live load case 1 (left), and accidental concentrated load case 2 (right); both with factored load values.Stress results are given in MPa, with positive values indicating tensile stresses. Stresses remain below the design strength values (3.5 MPa for tensile bending stresses across print layers, see Appendix).

These load cases were applied at critical locations of the blocks. For load cases type 1 and 2, these were the locations where spans between stiffeners were at their largest. For load case 3, the critical locations corresponded to the interfaces with the smallest areas - and hence the largest interface stresses. Load case 3 simulates an eventual hinged state where the load is applied only to a single edge of the 3DCP block, potentially causing buckling of the outer printed layer. However, in the case of Striatus, due to the connection of the outer layer to the stiffeners, the limited span between stiffeners, the local curvature of the outer layer

Fig. 31. Placing of the 3D-concrete-printed deck components on the waffle system.

Fig. 32. Placing of the 3D-concrete-printed balustrade components on the waffle system.

Fig. 33. Striatus before the lowering of the falsework. The gaps between the blocks are still visible, showing the arch is not yet standing by itself.

and the low compressive stresses, the section of the outer layer never had a high enough slenderness to be governed by out-of-plane buckling.

As an example of the results, Fig. 23 shows principal stress plots for a pentagonal deck block under punching load cases 1 and 2. Note that the global compression due to arching is disregarded here - a conservative assumption, as it would decrease the effective tensile stresses.

Finally, shear stresses were verified to remain within the material design capacity under local punching corresponding to load cases 1 and 2. As can be seen in Fig. 24, two print layers were used for the top surface of the deck blocks - the side taking all live loads - while one layer sufficed

Table A1
3D concrete printed material properties.

Mechanical properties of the 3D printed concrete after 28 days	
Characteristic compressive strength	75 [MPa]
Minimum mean compressive strength	80 [MPa]
Characteristic tensile strength from 4 points bending test: Transversal	3.5 [MPa]
Characteristic tensile strength from 4 points bending test: Longitudinal	5.5 [MPa]
Minimum Mean Young's modulus	42 [GPa]
Poisson's ratio	0.21
Density	2400 kg/m^3

Table A2
3D concrete printed material properties.

Mechanical properties of the Neoprene pads	
Material	CR/SBR
Hardness	50 ± 5 Shore A
Density	1.31 g/cm^3
Working Temperature range	from −20 to + 70 ℃

for the rest of the block's perimeter.

4. Foundation system

The foundation system is composed of steel footings connected by tension ties and bolted to reinforced concrete platforms anchored into the ground using ground screws (Fig. 25). The horizontal thrust generated by Striatus is transferred to the steel footings and then taken by the tension ties, which close the loop of the "arch" structural system. The steel supports follow the shape of the last 3D-printed block, and have been designed to form a supporting condition orthogonal to the resultant forces due to the self-weight of the funicular structure (Fig. 26). The tension ties are made of steel bands bolted to the support plates and following the medial axis of the bridge's structure.

The steel footings were installed on reinforced concrete pads with a thickness varying between 15 and 20 cm. Due to the poor quality of the soil in the garden, six ground screws per foundation pad were installed. Each ground screw was 0.55 m long, with a diameter of 0.089 m, and its head was connected to the steel reinforcement cage of the concrete pads, as shown in Fig. 27. The ground screws provided extra load-bearing capacity in the vertical direction, and due to their spatial placement and inclination, they could prevent any rotation of the supports caused by eventual resultant asymmetric forces.

As mentioned, the tension ties resolve the horizontal thrust generated by the arch bridge system. They were placed and bolted to the steel footings before the assembly of the 3D-printed components, using wooden blocks underneath the singularities to avoid sagging (Fig. 28). After the 3D-concrete-printed blocks were placed, the ties were activated by allowing slight outward movements of the steel supports, thanks to slotted holes receiving the steel anchors bars embedded in the foundation pads. Only after this activation due to the thrust of the structure, were the supports fixed by tightening the top nuts to the anchor bars.

The foundation system of Striatus was conceived with the clear design intent of exposing the tension ties in order to highlight the key structural principle of a "tied arch" and the separation between compression and tension. Regarding the addition of ground screws and the dimensioning of the concrete pads, in the case of Striatus, they considered the archaeological restrictions and the poor mechanical conditions of the soil in the Giardini della Marinaressa garden. However, depending on the constraints of the context, the foundation system could be solved differently, avoiding the redundancy (ties, ground screws, steel supports and concrete pads) present in Striatus. If allowed by the boundary conditions and depending on the design objectives, several solutions can be combined, e.g., i) only tension ties and reinforced concrete blocks; ii) only reinforced concrete blocks with a foundation able to take thrusts; iii) only reinforced concrete blocks and ground screws, etc.

5. Assembly

Funicular URM structures always require specific strategies for their assembly. The challenges are mainly due to the curvature of the geometry and the decentering strategy to activate the structure in compression. The following sections describe the assembly strategy adopted in this project.

5.1. Falsework system

In the case of Striatus, the falsework system was composed of a CNC laser-cut wooden waffle, shaped following the bridge's intrados. The waffle was supported by an adjustable scaffolding system made of standard steel DOKA components. The DOKA elements were placed on wooden planks directly on the ground and braced diagonally forming stable scaffolding towers. On the top of these, timber beams were inserted to carry the wooden waffles. Towers of different heights were used to step-wise approximate the curved profile of the bridge and thus reduce the needed depth of the wooden waffle. The scaffolding system was designed keeping in mind that the entire falsework structure had to be lowered carefully during the decentering, but also that local adjustments had to be possible in order to deal with site and assembly tolerances (Fig. 29).

The wooden waffle was designed to describe the intrados of the bridge, supporting both deck and balustrade components. It was made of OSB panels with a thickness of 18 mm. Slots and references were laser-cut to assemble the interlocking sheets into the waffle parts. (Fig. 30**a-b**).

5.2. Assembly sequence

The assembly sequence of Striatus started with the installation of the scaffolding system after the casting of the reinforced concrete pads. In this phase, the steel supports' position on the reinforced concrete pads was measured and only partially installed (see Section 4). Once the scaffolding system was assembled and the steel footings placed, the components of the wooden waffle were mounted and placed on top of it. Later, the tension ties were connected (bolted) to the footings, keeping the possibility of the steel fittings to slightly move outwards. After positioning the waffle, firstly, the deck components were placed in the central area of the falsework (Fig. 31), and, secondly, the balustrade blocks were added to the lateral sides (Fig. 32).

5.3. Decentering strategy

The decentering was done in two steps:

1. lowering and activation of the deck; and,
2. lowering and activation of the balustrade arches.

This strategy was accomplished by a specific design of the waffle's top surface with features to locate the deck and the balustrade blocks. The parts corresponding to the balustrades were designed slightly higher than the area receiving the deck blocks. In this way, as soon as the lowering started, the deck got activated sooner than the balustrade arches, which needed further lowering to close the gaps, touch the deck and reach equilibrium (Fig. 33**)**. The decentering of the scaffolding system was done evenly, lowering the DOKA elements in multiple locations. The activation of the bridge's structure during the decentering was monitored by observing the state of wooden shims used during the placement of the blocks. After the arch bridge was activated, and this standing by itself, the structure was left to "rest" for an entire day, keeping the scaffolding system below it at a certain distance, in case some instabilities would still occur.

6. Conclusions

This project demonstrated that applying URM structural principles to 3D-concrete-printed (3DCP) structures allows overcoming some of the current limitations of the technology, opening up the design space to structural elements able to span space horizontally. Moreover, it shows how the URM structural logic suits the mechanical properties of the printed material, able to take compressive forces with negligible tensile capacity, well. Vice versa, robotic 3DCP fulfils the requirements of URM regarding stereotomy and discretisation, which are fundamental for the global equilibrium of the structure.

In terms of sustainability, by combining an URM logic and 3DCP, this project achieves several targets:

- The additive manufacturing process allows for the application of the material only where it is needed. Indeed, in this project, the 3DCP components present a 40% empty cross-section, drastically reducing the material consumption;
- The material is also saved thanks to the funicular URM logic. In a compression-only structure and with a material well behaving in compression, the cross-section can be minimised since no bending has to be taken into account;
- Moreover, the compression-only principle perfectly suits the mechanical properties of the 3DCP material, which has no steel reinforcements. This enables easy recyclability of the printed components to produce new concrete afterwards; and,
- By applying pure URM structural principles on the discretisation and stereotomy, keeping the joints between the elements as perpendicular as possible to the flow of forces, dry joints can be used, hitting the concept of reusability. Indeed, the entire structure can be disassembled and reused with the same components without requiring new structural elements.

The realisation of Striatus has been made possible by the computational pipeline employed, from its design to its fabrication phase, developed in COMPAS. The computational workflow allowed the management of the complex 3D geometry through data structures and to interface multiple structural solvers for the form finding and global equilibrium analysis of discretised URM structures. Furthermore, the flexibility of the implemented pipeline and the benefits of the established COMPAS infrastructure represent an opportunity to further investigate the design of structural elements combining URM and 3DCP.

As mentioned, further investigation is ongoing to improve aspects related to the assembly sequence, the carbon footprint of the concrete inks and the overall structural performance as mostly influenced by the discretisation. The main goal is to improve the assembly onsite and reduce the amount of secondary materials such as wood and steel. Striatus demonstrated the potential of applying URM principles together with the newest digital fabrication technologies to tackle some of the challenges in the AEC industry, pushing the boundaries of 3D concrete printing.

CRediT authorship contribution statement

A. Dell'Endice: Conceptualization, Methodology, Software, Formal analysis, Investigation, Data curation, Writing – original draft, Writing – review & editing, Visualization. **S. Bouten:** Conceptualization, Methodology, Validation, Formal analysis, Software, Writing – review & editing. **T. Van Mele:** Conceptualization, Resources, Supervision, Validation, Software. **P. Block:** Conceptualization, Resources, Supervision, Validation, Writing – review & editing.

Declaration of Competing Interest

The authors declare that they have no known competing financial interests or personal relationships that could have appeared to influence the work reported in this paper.

Data availability

Data will be made available on request.

Acknowledgements

The project team for the physical demonstrator was multidisciplinary and comprised many more contributors. The full project credits are listed below:

Design

ZHACODE: Jianfei Chu, Vishu Bhooshan, Henry David Louth, Shajay Bhooshan, Patrik Schumacher.

ETHZ BRG: Tom Van Mele, Alessandro Dell'Endice, Philippe Block.

Structural engineering.

ETHZ BRG: Tom Van Mele, Alessandro Dell'Endice, Sam Bouten, Philippe Block.

Fabrication Design.

ETHZ BRG: Shajay Bhooshan, Alessandro Dell'Endice, Sam Bouten, Chaoyu Du, Tom Van Mele.

ZHACODE: Vishu Bhooshan, Philip Singer, Tommaso Casucci.

3D concrete printing.

incremental3D: Johannes Megens, Georg Gasser, Sandro Sanin, Nikolas Janitsch, Janos Mohacsi.

Concrete material development.

Holcim: Christian Blachier, Marjorie Chantin-Coquard, Hélène Lombois-Burger, Francis Steiner.

LafargeHolcim Spain: Benito Carrión, José Manuel Arnau.

Assembly and Construction.

Bürgin Creations: Theo Bürgin, Semir Mächler, Calvin Graf.

ETHZ BRG: Alessandro Dell'Endice, Tom Van Mele.

Logistics.

ETHZ BRG: Alessandro Dell'Endice, Tom Van Mele.

Holcim Switzerland and Italy: Michele Alverdi.

LafargeHolcim Spain: Ricardo de Pablos, José Luis Romero.

Additional partners.

Ackermann GmbH [CNC timber formwork]

L2F Architettura [site measurements]

Pletscher [steel supports]

ZB Laser [lasercutting neoprene]

Documentation.

ZHACODE: Jianfei Chu,Edward Meyers, Cesar Fragachan, Philip Singer, Vishu Bhooshan, Shajay Bhooshan ETHZ BRG: Tom Van Mele, Alessandro Dell'Endice, Philippe Block.

incremental3D: Alexander Gugitscher, Sandro Sanin, Nikolas Janitsc.

LBS Fotografia.

Naaro

Appendix

A.1 Material properties

A.1.1 3D printed concrete

In the 3D-concrete-printing process, the available ready-to-use mix was used, which corresponds to a high-strength mix with additives to optimise flowability, slump, curing times and shrinkage. The mix was produced by Holcim, who also tested the material and provided the data sheet with the characteristic values of the most important mechanical properties (Table A.1).

Due to the fabrication process, the material is orthotropic on a macro-level, as the deposition in layers ensures a stronger bond in the direction perpendicular to the printed layers than between adjacent layers. This is reflected in the two values for the characteristic tensile-flexural strengths (transversal and longitudinal directions, respectively). It should be noted that the actual design compressive stresses are much lower than the characteristic compressive strength of the material (75 MPa). More important for the local structural checks is the flexural-tensile strength, which has been considered in the FEM analysis of the layer's thickness and stiffener spacing.

A.2 Neoprene pads

The neoprene pads at the interfaces between the blocks had two different thicknesses (6 and 8 mm) as already described in Par. 2.4.1. However, both types of the neoprene share the same material properties, Table A.2.

References

[1] Roussel N. Rheological requirements for printable concretes. Cem Concr Res 2018; 112:76–85. https://doi.org/10.1016/j.cemconres.2018.04.005.

[2] Sanjayan JG, Nematollahi B, Xia M, Marchment T. Effect of surface moisture on inter-layer strength of 3D printed concrete. Constr Build Mater 2018;172:468–75. https://doi.org/10.1016/j.conbuildmat.2018.03.232.

[3] Wolfs RJM, Bos FP, Salet TAM. Hardened properties of 3D printed concrete: The influence of process parameters on interlayer adhesion. Cem Concr Res 2019;119: 132–40. https://doi.org/10.1016/j.cemconres.2019.02.017.

[4] Nerella VN, Hempel S, Mechtcherine V. Effects of layer-interface properties on mechanical performance of concrete elements produced by extrusion-based 3D-printing. Constr Build Mater 2019;205:586–601. https://doi.org/10.1016/j.conbuildmat.2019.01.235.

[5] Wolfs RJM, Bos FP, Salet TAM. Early age mechanical behaviour of 3D printed concrete: Numerical modelling and experimental testing. Cem Concr Res 2018;106: 103–16. https://doi.org/10.1016/j.cemconres.2018.02.001.

[6] Le TT, Austin SA, Lim S, Buswell RA, Law R, Gibb AGF, et al. Hardened properties of high-performance printing concrete. Cem Concr Res 2012;42:558–66. https://doi.org/10.1016/j.cemconres.2011.12.003.

[7] Le TT, Austin SA, Lim S, Buswell RA, Gibb AGF, Thorpe T. Mix design and fresh properties for high-performance printing concrete. Mater Struct 2012;45:1221–32. https://doi.org/10.1617/s11527-012-9828-z.

[8] Li Z, Hojati M, Wu Z, Piasente J, Ashrafi N, Duarte JP, et al. Fresh and Hardened Properties of Extrusion-Based 3D-Printed Cementitious Materials: A Review. Sustainability 2020;12:5628. https://doi.org/10.3390/su12145628.

[9] Lee H, Kim J-H-J, Moon J-H, Kim W-W, Seo E-A. Evaluation of the Mechanical Properties of a 3D-Printed Mortar. Materials 2019;12:4104. https://doi.org/10.3390/ma12244104.

[10] Khoshnevis B. Automated construction by contour crafting—related robotics and information technologies. Autom Constr 2004;13:5–19. https://doi.org/10.1016/j.autcon.2003.08.012.

[11] Hwang D, Khoshnevis B. Concrete Wall Fabrication by Contour Crafting, 2004. 10.22260/ISARC2004/0057.

[12] Bos FP, Ahmed ZY, Wolfs RJM, Salet TAM. 3D Printing Concrete with Reinforcement. High Tech Concrete: Where Technology and Engineering Meet. Cham: Springer International Publishing; 2018. p. 2484–93.

[13] Anton ANA, Bedarf P, Yoo A, Dillenburger B, Reiter LEX, Wangler T, et al. CONCRETE CHOREOGRAPHY. In: PREFABRICATION OF 3D-PRINTED COLUMNS. Fabricate 2020: Making Resilient Architecture. UCL Press; 2020. p. 286–93.

[14] Xu W, Gao Y, Sun C, Wang Z. Fabrication and Applications of 3D-Printed Concrete Structural Components in the Baoshan Pedestrian Bridge Project. Fabricate 2020. UCL Press; 2020. p. 140–7.

[15] Salet TAM, Ahmed ZY, Bos FP, Laagland HLM. Design of a 3D printed concrete bridge by testing. Virtual Phys Prototyp 2018;13:222–36. https://doi.org/10.1080/17452759.2018.1476064.

[16] Carneau P, Mesnil R, Roussel N, Baverel O. An exploration of 3d printing design space inspired by masonry, 2019. 10.5281/zenodo.3563672.

[17] Carneau P, Mesnil R, Roussel N, Baverel O. Additive manufacturing of cantilever - From masonry to concrete 3D printing. Autom Constr 2020;116:103184. https://doi.org/10.1016/j.autcon.2020.103184.

[18] Motamedi M, Oval R, Carneau P, Baverel O. Supportless 3D Printing of Shells: Adaptation of Ancient Vaulting Techniques to Digital Fabrication. In: Impact: Design With All Senses. Cham: Springer International Publishing; 2020. p. 714–26. https://doi.org/10.1007/978-3-030-29829-6_55.

[19] Gebhard L, Mata-Falcón J, Anton A, Dillenburger B, Kaufmann W. Structural behaviour of 3D printed concrete beams with various reinforcement strategies. Eng Struct 2021;240:112380. https://doi.org/10.1016/j.engstruct.2021.112380.

[20] Gebhard L, Mata-Falcón J, Markić T, Kaufmann W. Aligned Interlayer Fibre Reinforcement for Digital Fabrication with. Concrete 2021:87–98. https://doi.org/10.1007/978-3-030-58482-5_8.

[21] Tam K-MM, Mueller KT, Coleman JR, Fine NW. Stress Line Additive Manufacturing (SLAM) for 2.5-D Shells. Journal of the International Association for Shell and Spatial Structures 2016;57:249–59. 10.20898/j.iass.2016.190.856.

[22] Tam K-M-M, Mueller CT. Additive Manufacturing Along Principal Stress Lines 2017;4:63–81. 3D.

[23] Bedarf P, Dutto A, Zanini M, Dillenburger B. Foam 3D printing for construction: A review of applications, materials, and processes. Autom Constr 2021;130:103861. https://doi.org/10.1016/j.autcon.2021.103861.

[24] Bos FP, Menna C, Pradena M, Kreiger E, da Silva WRL, Rehman AU, et al. The realities of additively manufactured concrete structures in practice. Cem Concr Res 2022;156:106746. https://doi.org/10.1016/j.cemconres.2022.106746.

[25] Bhooshan S, Van Mele T, Block P. Equilibrium-aware shape design for concrete printing. In: Humanizing Digital Reality - Proceedings of the Design Modelling Symposium 2017. Paris: Springer; 2018. p. 493–508. https://doi.org/10.1007/978-981-10-6611-5_42.

[26] Mesnil R, Poussard V, Sab K, Caron J-F. On the geometrical origin of the anisotropy in extrusion-based 3d printed structures. Eng Struct 2023;275:115082. https://doi.org/10.1016/j.engstruct.2022.115082.

[27] Bhooshan S, Bhooshan V, Dell'Endice A, Megens J, Chu J, Singer P, et al. The Striatus arched bridge: Computational design and robotic fabrication of an unreinforced, 3D-concrete-printed, masonry bridge. Structures and Construction: Architecture; 2022.

[28] Bhooshan S., Bhooshan V., Megens J., Casucci T., Van Mele T., Block P. Print-path design for inclined-plane robotic 3D printing of unreinforced concrete. In: Gengnagel C.B.O.B.G.P.M.T.M.R.W.J., editor. Design Modelling Symposium. Berlin 2022: Towards Radical Regeneration; 2022. doi:10.1007/978-3-031-13249-0_16.

[29] Heyman J. The stone skeleton. Int J Solids Struct 1966. https://doi.org/10.1016/0020-7683(66)90018-7.

[30] Van Mele T, Liew A, Mendez Echenagucia T, Rippmann M, others. COMPAS. A framework for computational research in architecture and structures. Block Research Group 2017;1:2018.

[31] Dell'Endice A. Structural Assessment and Design of Unreinforced Masonry Structures using Discrete Element Modelling 2023. https://doi.org/10.3929/ETHZ-B-000596377.

[32] Itasca Consulting Group Inc. 3DEC — Three-Dimensional Distinct Element Code, Ver. 5.2. Minneapolis: Itasca 2016.

[33] Cundall PA. Formulation of a three-dimensional distinct element model-Part I. A scheme to detect and represent contacts in a system composed of many polyhedral blocks. International Journal of Rock Mechanics and Mining Sciences And 1988. https://doi.org/10.1016/0148-9062(88)92293-0.

[34] Hart R, Cundall PA, Lemos J. Formulation of a three-dimensional distinct element model-Part II. Mechanical calculations for motion and interaction of a system composed of many polyhedral blocks. International Journal of Rock Mechanics and Mining Sciences And 1988. https://doi.org/10.1016/0148-9062(88)92294-2.

[35] Iannuzzo A, Dell'Endice A, Maia Avelino R, Kao GTC, Van Mele T, Block P. COMPAS Masonry: a computational framework for practical assessment of unreinforced masonry structures. Proceedings of the SAHC Symposium 2020;2020.

[36] Lemos J. DISCRETE ELEMENT MODELING OF MASONRY STRUCTURES 2007; 3058. 10.1080/15583050601176868.

[37] Lemos J v. The Basis for Masonry Analysis with UDEC and 3DEC, 2016, p. 61–89. 10.4018/978-1-5225-0231-9.ch003.

[38] DeJong MJ, Vibert C. Seismic response of stone masonry spires: Computational and experimental modeling. Eng Struct 2012. https://doi.org/10.1016/j.engstruct.2012.03.001.

[39] McInerney J, DeJong MJ. Discrete Element Modeling of Groin Vault Displacement Capacity. International Journal of Architectural Heritage 2015. https://doi.org/10.1080/15583058.2014.923953.

[40] Block P, Van Mele T, Liew A, DeJong M, Escobedo D, Ochsendorf J. Structural design, fabrication and construction of the Armadillo vault. Structural Engineer 2018;96.

[41] Van Mele T, Mehrotra A, Mendez Echenagucia T, Frick U, Ochsendorf JA, DeJong MJ, et al. Form finding and structural analysis of a freeform stone vault. Proceedings of the IASS Annual Symposium 2016 "Spatial Structures in the 21st Century". 2016.

[42] Simon J, Bagi K. Discrete Element Analysis of the Minimum Thickness of Oval Masonry Domes. International Journal of Architectural Heritage 2016. https://doi.org/10.1080/15583058.2014.996921.

[43] Sarhosis V, Lemos JV, Bagi K. Discrete element modeling. Numerical Modeling of Masonry and Historical Structures. Elsevier 2019:469–501. https://doi.org/10.1016/b978-0-08-102439-3.00013-0.

[44] Block P. Thrust Network Analysis: Exploring Three-dimensional Equilibrium. PhD Thesis 2009.

[45] Block P, Ochsendorf J. Thrust network analysis: A new methodology for three-dimensional equilibrium. Journal of the International Association for Shell and Spatial Structures 2007;48:167–73.

[46] Van Mele T, Panozzo D, Sorkine-Hornung O, Block P. Best-fit Thrust Network Analysis - Rationalization of freeform meshes. In: Adriaenssens S, Block P, Veenendaal D, Williams C, editors. Shell Structures for Architecture: Form Finding and Optimization. London: Routledge; 2014.

[47] Magliulo G, Capozzi V, Fabbrocino G, Manfredi G. Neoprene–concrete friction relationships for seismic assessment of existing precast buildings. Eng Struct 2011; 33:532–8. https://doi.org/10.1016/j.engstruct.2010.11.011.

[48] Van Mele T, McInerney J, DeJong MJ, Block P. Physical and Computational Discrete Modelling of Masonry Vault Collapse. Structural Analysis of Historical Constructions 2012;1–3:2552–60.

[49] Dell'Endice A, Iannuzzo A, DeJong MJ, Van Mele T, Block P. Modelling imperfections in unreinforced masonry structures: Discrete Element simulations and scale model experiments of a pavilion vault. Eng Struct 2021;228.
[50] NTC (2018) Supplemento ordinario alla Gazzetta Ufficiale, n. 42 del 20 Febbraio 2018. Ministero delle Infrastrutture e dei Trasporti, Ministerial Decree DM 17 Gennaio 2018, n.d.
[51] SOFiSTiK AG. SOFiSTiK analysis programs version 2020., 2020.